

Spectral comparison of weak short bursts to the persistent X-rays from the magnetar 1E 1547.0–5408 in its 2009 outburst

T. Enoto,^{1,2★} Y. E. Nakagawa,³ T. Sakamoto² and K. Makishima^{1,4}

¹High Energy Astrophysics Laboratory, Institute of Physical and Chemical Research (RIKEN), Wako, Saitama, 351-0198, Japan

²Goddard Space Flight Center, NASA, Greenbelt, Maryland, 20771, USA

³Research Institute for Science and Engineering, Waseda University, 17 Kikui-cho, Shinjuku-ku, Tokyo 162-0044, Japan

⁴Department of Physics, University of Tokyo, 7-3-1 Hongo, Bunkyo-ku, Tokyo, 113-0033, Japan

Accepted 2012 September 7. Received 2012 August 23; in original form 2011 December 8

ABSTRACT

In 2009 January, the 2.1-s anomalous X-ray pulsar 1E 1547.0–5408 evoked intense burst activity. A follow-up *Suzaku* observation on January 28 recorded enhanced persistent emission in both soft and hard X-rays. Through a reanalysis of the same *Suzaku* data, 18 short bursts were identified in the X-ray events recorded by the Hard X-ray Detector (HXD) and the X-ray Imaging Spectrometer (XIS). Their spectral peaks appear in the HXD–PIN band, and their 10–70 keV X-ray fluences range from $\sim 2 \times 10^{-9}$ to 10^{-7} erg cm⁻². Thus, the 18 events define a significantly weaker burst sample than has ever been obtained previously, $\sim 10^{-8}$ – 10^{-4} erg cm⁻². In the ~ 0.8 to ~ 300 keV band, the spectra of the three brightest bursts can be represented successfully by a two-blackbody model, or a few alternative models. A spectrum that is constructed by stacking 13 weaker short bursts with fluences in the range $(0.2\text{--}2) \times 10^{-8}$ erg s⁻¹ is less curved, and its ratio to the persistent emission spectrum becomes constant at ~ 170 above ~ 8 keV. As a result, the two-blackbody model was able to reproduce the stacked weaker-burst spectrum only after adding a power-law model, for which the photon index is fixed at 1.54 as measured by the persistent spectrum. These results imply that there is a possibility that the spectrum composition that employs an optically thick component and a hard power-law component can describe the wide-band spectra of both the persistent and weak-burst emissions, despite the fact that their fluxes differ by two orders of magnitude. Based on the spectral similarity, we discuss a possible connection between the unresolved short bursts and the persistent emission.

Key words: stars: magnetars – pulsars: individual: 1E 1547.0–5408 – pulsars: individual: SGR J1550–5418 – pulsars: individual: PSR J1550–5418 – pulsars: individual: G327.24–013 – ISM: supernova remnant.

1 INTRODUCTION

Magnetars are a peculiar subclass of isolated neutron stars (Duncan & Thompson 1992; Thompson & Duncan 1995) with evidence of ultra-strong magnetic fields, mainly emitting in the X-ray frequency. Located along the Galactic plane and in the Magellanic Clouds, \sim nine soft gamma repeaters (SGRs) and \sim 12 anomalous X-ray pulsars (AXPs) are currently believed to be of the magnetar class (for reviews, see Woods & Thompson 2006; Mereghetti 2008). X-ray pulsations have been observed from these in a period range of $P = 2\text{--}12$ s, indicating slowly rotating isolated pulsars. Together with their large period derivatives $\dot{P} \sim 10^{-12}\text{--}10^{-10}$ s s⁻¹, the magnetic-dipole-radiation approximation indicates that these objects have

ultra-strong magnetic fields of $B = 3.2 \times 10^{19} \sqrt{P\dot{P}} \gtrsim 3.3 \times 10^{13}$ G. Thus, it is widely believed that the peculiar characteristics of SGRs and AXPs originate from their extremely strong magnetic fields.

The X-ray radiation from magnetars emerges on a large variety of time-scales and intensities. One form is persistent X-ray emission with a typical luminosity of $L_X \sim 10^{35}$ erg s⁻¹, which is usually stable over long periods of time (\sim a few months or longer). A typical persistent X-ray luminosity of magnetars exceeds by one to two orders of magnitude that available from their rotational energy losses, $\sim 10^{33}\text{--}10^{34}$ erg s⁻¹. Without evidence of mass accretion, the emission is considered to be powered by the dissipation of the magnetic energies. The broad-band persistent X-ray spectrum is generally composed of a blackbody-like soft X-ray component, with a temperature of $\sim 0.3\text{--}0.5$ keV (Rea et al. 2007; Mereghetti 2008; Enoto et al. 2011), and a power-law-like hard X-ray component,

★E-mail: teru.enoto@riken.jp

with a photon index of $\Gamma \sim 1$ (Kuiper et al. 2006; den Hartog et al. 2008; Enoto et al. 2010c). While the soft component can be considered as optically thick thermal radiation from the stellar surface, the hard component, spanning from ~ 10 to ~ 200 keV or higher, is considered to emerge through a different and yet unidentified process (e.g. Heyl & Hernquist 2005; Thompson & Beloborodov 2005; Baring & Harding 2007; Beloborodov & Thompson 2007; Fernández & Thompson 2007).

Another form of X-ray radiation from magnetars is a sporadic emission of bursts with a typical duration from ~ 0.1 s to a few hundred seconds. These bursts are phenomenologically classified into three types: quite rare giant flares, with $L_X \gtrsim 10^{45}$ erg s $^{-1}$, lasting for about a few hundred seconds (Mazets et al. 1979; Feroci et al. 2001; Hurley et al. 2005); intermediate flares, with $L_X \sim 10^{42}$ – 10^{43} erg s $^{-1}$, lasting a few seconds (Kouveliotou et al. 2001; Olive et al. 2004; Israel et al. 2008); and much more frequently occurring short bursts, with $L_X \sim 10^{38}$ – 10^{41} erg s $^{-1}$ and durations of ~ 0.1 s (Nakagawa et al. 2007; Israel et al. 2008). Thus, these explosive events often show luminosities exceeding the Eddington limit for a neutron star of $1.4 M_\odot$ (where M_\odot is the solar mass), $L_{\text{Edd}} \sim 1.8 \times 10^{38}$ erg s $^{-1}$, presumably because of the suppression of the electron scattering cross-sections in the strong field (Paczynski 1992). The mechanisms of these bursts are thought to be related to the rearrangement of the magnetic fields invoking reconnection (Lyutikov 2003), or to the motion and fracturing of the neutron star crust (i.e. starquake; Thompson, Lyutikov & Kulkarni 2002).

The persistent X-ray intensity of a magnetar sometimes increases by one to two orders of magnitude with unpredictable timing. Such a transient enhancement lasts typically for a few months, including its gradual decay. It is often accompanied, in its early phase, by a burst activity, which can even lead to discoveries of new magnetars. Such burst-active states, or outbursts, have already been observed from some magnetars; XTE J1810–197 (Gotthelf et al. 2004; Ibrahim et al. 2004; Israel et al. 2004; Gotthelf & Halpern 2005; Bernardini et al. 2009), CXOU J164710.2–455216 (Israel et al. 2007; Munro et al. 2007), SGR 0501+4516 (Enoto et al. 2009; Rea et al. 2009; Enoto et al. 2010a) and 1E 1547.0–5408 (Mereghetti et al. 2009; Enoto et al. 2010b, hereafter Paper I). More recently, there have been increasing numbers of reports concerning such activities from sources with much weaker dipole fields ($\lesssim 4.4 \times 10^{13}$ G): SGR 0418+5729 (Rea et al. 2010; van der Horst et al. 2010), SGR 1833–0832 (Göğüş et al. 2010a; Esposito et al. 2011), Swift J1822.3–1606 (Rea et al. 2012) and Swift J1834.9–0846 (Kargaltsev et al. 2012).

The enhanced persistent emission and the burst activity have been simultaneously observed in many activated magnetars. However, it is not yet clear how these two forms of emission are physically related to each other in the postulated dissipation process of the magnetic energy. One interesting possibility is that the persistent emission is composed of a large number of small bursts that cannot be detected individually (e.g. Thompson & Duncan 1996; Lyutikov 2003; Nakagawa 2007). Such a possibility has been examined using a cumulative number-intensity distribution of short bursts (Götz et al. 2006; Nakagawa et al. 2007). However, the observational information has so far remained insufficient to evaluate this possibility, because the studied short bursts are so bright (with fluence $\gtrsim 10^{-7}$ erg cm $^{-2}$) and infrequent that their time-averaged flux is much lower than that of the persistent emission. Therefore, it is interesting to examine, from observations of activated magnetars, whether weaker short bursts become similar in spectral shape to the persistent X-ray emission, as recently found for SGR 0501+4516 (Nakagawa, Makishima & Enoto 2011).

In this paper, we study the activated magnetar 1E 1547.0–5408. Following its discovery by the *Einstein Observatory* (Lamb & Markert 1981) in 1980, and confirmation by *ASCA* (Sugizaki et al. 2001), this object has been recognized as a magnetar candidate, located at the centre of the supernova remnant G327.24–013 (Gelfand & Gaensler 2007), based on its X-ray spectrum from *XMM-Newton* and *Chandra* observations. This was followed by the discovery of its radio pulsations at ~ 2.07 s (PSR J1550–5418; Camilo et al. 2007), and of X-ray pulsations at the same period (Halpern et al. 2008). Together with a measured period derivative, $\dot{P} \sim 2.3 \times 10^{-11}$ s s $^{-1}$ (Camilo et al. 2007), its characteristic age and surface magnetic field intensity were estimated to be 1.4 kyr and 2.2×10^{14} G, respectively; both parameters fall in the magnetar regime. At present, 1E 1547.0–5408 is one of the fastest rotating objects among the known magnetars.

Fig. 1 shows the long-term monitoring of the 2–10 keV persistent emission from 1E 1547.0–5408. In 2007, a small enhancement was observed in its persistent luminosity (Halpern et al. 2008). In 2008 October, short bursts and decaying persistent soft X-rays were monitored by *Swift* (Israel et al. 2010). Three months later, a much stronger burst activity, which we deal with in this paper, was detected on 2009 January 22 (UT). A series of intense short bursts were recorded by several satellites: *Swift* (Gronwall et al. 2009), *INTEGRAL* (Savchenko et al. 2009), *Suzaku* (Terada et al. 2009), the *Fermi*/Gamma-ray Burst Monitor (GBM; Connaughton & Briggs 2009; von Kienlin & Connaughton 2009), the *Reuven Ramaty High Energy Solar Spectroscopic Imager* (RHESSI; Bellm, Smith & Hurley 2009) and *Konus-Wind* (Golenetskii et al. 2009). Some bursts were very bright, with fluences above $\sim 10^{-5}$ erg cm $^{-2}$ (Mereghetti et al. 2009), and a 150-s-long enhanced quasi-persistent emission was also recorded on one occasion by the *Fermi*/GBM (Kaneko et al. 2010). Based on these SGR-like activities, 1E 1547.0–5408 has also been named SGR J1550–5418 (Kouveliotou et al. 2009).

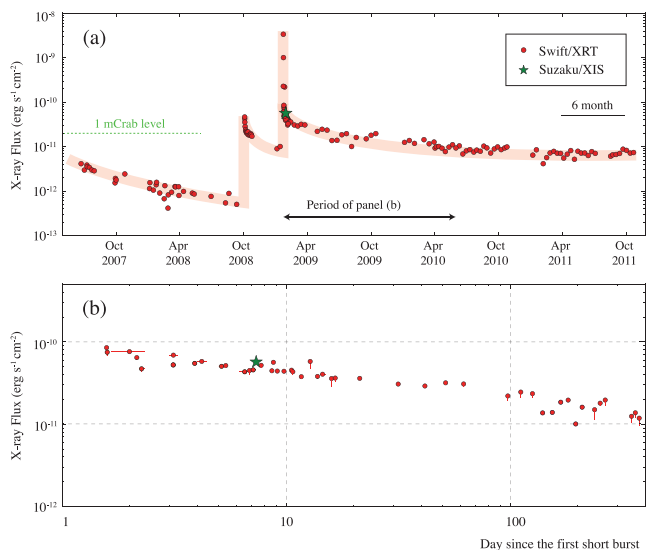


Figure 1. Long-term X-ray monitoring of 1E 1547.0–5408 with the *Swift*/XRT, produced from the public *Swift* data archive through a standard analyses procedure, fitted by an absorbed BB spectrum with the absorption left free. (a) The absorbed 2–10 keV X-ray flux since 2007 May is shown. The *Suzaku* observation is shown by the star (green). (b) An expanded view of panel (a) during the 2009 outburst. The decay is shown as a double logarithmic plot since the first short burst (2009-01-22 01:32:41; Gronwall et al. 2009).

As shown in Fig. 1, the early burst activity was accompanied by a clear enhancement of the persistent emission, which decayed on a time-scale of a few months. In Paper I, we studied the persistent emission of this object using the *Suzaku* data acquired on 2009 January 28–29, or ~ 7 d after the burst onset (Fig. 1), when the 2–10 keV persistent flux became one to two orders of magnitude higher than that during less active states in 2006 and 2007. On that occasion, a persistent hard X-ray component was detected for the first time from this source, at least up to ~ 110 keV. The acquired broadband spectrum in 0.7–114 keV was reproduced by an absorbed blackbody (BB) emission with a temperature of 0.65 ± 0.02 keV, plus a prominent hard power law (PL) with a photon index of $\Gamma_{\text{per}} \sim 1.5$. The enhanced persistent emission was also studied by *Chandra*, *XMM-Newton*, *Swift* and *INTEGRAL* (den Hartog, Kuiper & Hermsen 2009; Kuiper, den Hartog & Hermsen 2009; Bernardini et al. 2011; Ng et al. 2011).

In this paper, we present spectral studies of short bursts detected with *Suzaku* in the 2009 observations. The low background of *Suzaku*, especially in the hard X-ray band, has allowed us to detect much weaker short bursts than observed so far from any magnetars. Unless otherwise specified, we show all uncertainties at the 68 per cent (1σ) confidence level,

2 OBSERVATION AND DATA REDUCTION

2.1 Observation and data screening

We utilized the same *Suzaku* data (OBSID 903006010) of 1E 1547.0–5408 as used in Paper I, although short-burst events were eliminated therein. The data were acquired over ~ 1 d from 2009 January 28 21:34 (UT) to January 29 21:32 (UT). As described in Paper I, two (XIS1 and XIS3) among the three X-ray Imaging Spectrometer (XIS; Koyama et al. 2007) sensors were operated with a 1/4 window mode plus burst option, repeating a 0.5-s exposure and a 1.5-s artificial dead-time. The other sensor, XIS0, was operated in the timing mode (P-sum mode) to attain a high time resolution of ~ 7.8 ms, together with one-dimensional position information. The Hard X-ray Detector (HXD; Takahashi et al. 2007), composed of silicon PIN diodes (HXD-PIN; 10–70 keV) and GSO scintillators (HXD-GSO; ~ 50 –600 keV), was operated in the normal mode with 61 μ s time resolution. Effective exposures were 42.5, 10.6, 10.6 and 33.5 ks with XIS0, XIS1, XIS3 and the HXD, respectively.

The event-screening criteria of the HXD are the same as in Paper I, except for two conditions. We allow all geomagnetic cut-off rigidity (which was ≥ 6 GV in Paper I) and any data transfer criteria, in order to include as many short bursts as possible. These changes do not affect the signal-to-noise ratios of the short bursts, because they are almost free from the background as a result of their short duration ($\lesssim 1$ s).

We utilized standard filtered files for XIS1 and XIS3, while we started our XIS0 analyses from the unfiltered event file. These raw P-sum events were corrected and filtered in the way recommended by the XIS team (Matsuta et al. 2010), including corrections of PI values by the *FTOOL* software *XISPI*, selections with criteria of (GRADE==0 || GRADE==1 || GRADE==2) && (STATUS>=0 && STATUS<= 524287), and filtering with scripts of *XISREPRO.XCO* and *XIS_MKF.SEL*. We further eliminated apparent hot pixels from the XIS0 data, and corrected the P-sum mode timing for the known delay (31.2 ms in the present case), depending on the source location on the CCD chip.

Fig. 2 shows light curves of 1E 1547.0–5408 recorded with XIS0 (2–10 keV), XIS1+XIS3 (2–10 keV), HXD-PIN (10–70 keV) and

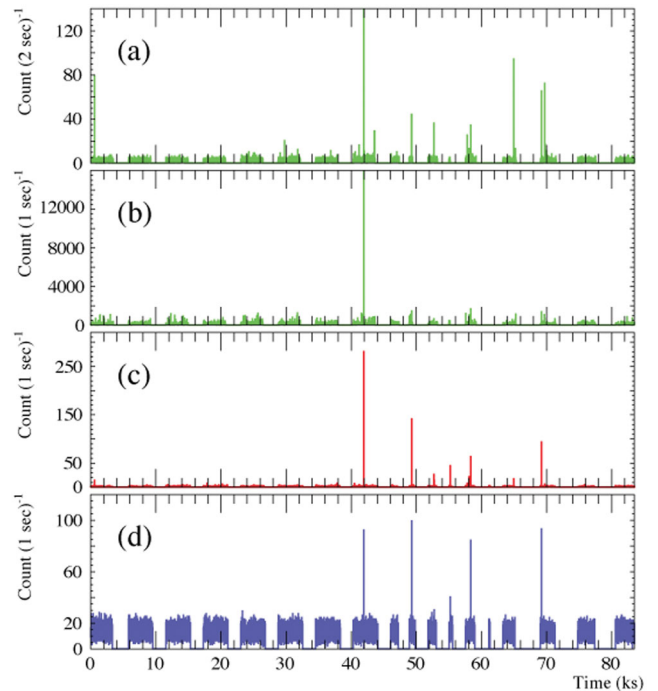


Figure 2. Background-inclusive count rates of 1E 1547.0–5408 during the present *Suzaku* observation performed on 2009 January 28. From top to bottom, the panels refer to observations obtained with XIS1 plus XIS3 (2–10 keV), XIS0 (2–10 keV), HXD-PIN (10–70 keV) and HXD-GSO (50–150 keV). Data are binned into 1 s, except for panel (a) which has bins of 2 s.

HXD-GSO (50–150 keV), which exhibit background-inclusive average count rates of 3.89, 5.77, 0.76 and 13.38 counts s^{-1} , respectively. Several short-burst events clearly appear in all light curves.

2.2 Identification of short bursts

The short bursts are characterized as bunched X-ray photons. In order to identify such bunched events, we have studied the distributions of delta-time (Δt), which is defined as the waiting times of individual X-ray photons (including background events) from the preceding events. In this study, we have utilized the 10–70 keV HXD-PIN data, because these have a better signal-to-noise ratio than those of HXD-GSO and XIS0, and a finer time resolution (61 μ s) than XIS0 (~ 7.8 ms). Besides, unlike the XIS1 or XIS3 data with burst options, HXD-PIN is free from periodic data gaps. The Δt analysis provides a standard method to identify bunched events, and is actually implemented in the HXD digital electronics (HXD-DE; see section 4.3 of Takahashi et al. 2007) to eliminate instrumental event bunching on time-scales of \lesssim a few ms.

Fig. 3(a1) shows the calculated Δt distribution of the 10–70 keV HXD-PIN data with a bin size of $t_{\text{bin}} = 7.8$ ms. A large portion of these events are non-X-ray background (NXB) events. The Δt values of such random events follow an exponential probability distribution, $P(\Delta t) \propto \exp(-\lambda \Delta t)$, where λ is the average event rate. The best-fitting exponential function, shown in Fig. 3(a1) by a dash-dotted line, gives $\lambda = 0.778 \pm 0.001$ count s^{-1} , which agrees well with the average count rate, 0.76 count s^{-1} , derived in Section 2.1. On closer inspection of Fig. 3(a2), the actual Δt distribution deviates from the best-fitting model below ~ 50 ms. This indicates that some events are bunched, with separations much shorter than λ^{-1} . Thus, we choose a threshold interval of $\Delta t_{\text{th}} \equiv 6 t_{\text{bin}} = 46.9$ ms to regard an event as possibly bunched. The chance

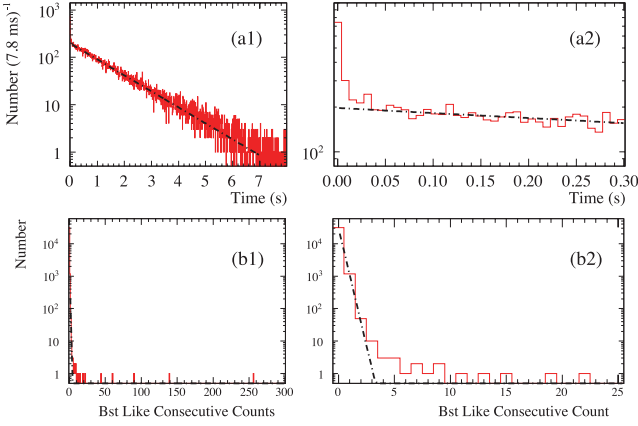


Figure 3. (a1) A Δt distribution of the 10–70 keV HXD-PIN events. The dashed-dotted line indicates the best-fitting exponential model with the average event rate of $\lambda = 0.778 \pm 0.001 \text{ count s}^{-1}$. (a2) An expanded view of panel (a1) in the 0–0.3 s range. (b1) Distribution of the consecutive burst-like counts calculated using panel (a). (b2) An expanded view of panel (b1). The dashed-dotted line represents the predicted chance coincidence probability of ordinary events, $(0.036)^{N_{\text{bst}}}$.

probability of observing $\Delta t \leq \Delta t_{\text{th}}$ is $[1 - \exp(-\lambda \Delta t_{\text{th}})] = 3.6$ per cent.

Under the above preparation, we define ‘an event train of length N_{bst} ’ as an event bunching where N_{bst} consecutive events are detected, all with a waiting time of $\Delta t < \Delta t_{\text{th}}$. Most NXB events sparsely occur with $\Delta t > \Delta t_{\text{th}}$, and hence with $N_{\text{bst}} = 0$. Because the chance occurrence of a bunching with length N_{bst} is simply $(0.036)^{N_{\text{bst}}}$, we estimate those with $N_{\text{bst}} = 3, 4$ and 5 as 4.7×10^{-5} , 1.7×10^{-6} and 6.0×10^{-8} , respectively. Considering the

10–70 keV total PIN events of $\sim 3.4 \times 10^4$ counts, chance detections of event trains with $N_{\text{bst}} = 3, 4$ and 5 during the entire observation become ~ 2 , ~ 0.06 and ~ 0.002 , respectively. Therefore, event trains with $N_{\text{bst}} \geq 4$ would be securely identified as short bursts. Compared to a more conventional way of detecting sudden increases in the light curve, this method is more suited to our search for weak bursts on two points: it is unaffected by count binning, and it works even when a burst has a gradual rise (e.g. with a precursor).

Fig. 3(b1) shows the N_{bst} distribution in comparison with the predicted chance coincidence probability of ordinary events, $(0.036)^{N_{\text{bst}}}$. We find data points with $N_{\text{bst}} \geq 4$, which deviate significantly from the fit, and hence we regard them as short bursts. We have further merged two separate bursts into one if they were detected within the adjacent 1 s. Using these criteria, we have successfully detected 18 short-burst events, as listed in Table 1.

To confirm these detections in an independent way, we have also studied distributions of the count rates in the light curves of Fig. 2. The calculated histograms are shown in Fig. 4. In Fig. 4(b), the short bursts appear as significant deviations from the best-fitting Poisson distribution, which is superposed as a solid curve. From Fig. 4(b), only 15 of the above 18 bursts can be recognized as 1-s bins where \geq eight events have been detected. Thus, both methods give almost the same detections. Further corrections for the XIS1 timing mode are described in Appendix A.

We have also searched the *Swift*/Burst Alert Telescope (BAT) data for possible detections of the same short bursts. Using the same trigger code as used by Graziani (2003) on the 64-ms BAT data, only two bursts were recorded by the BAT. This is mainly because the BAT, with its wide field of view, has a higher background. In other words, the HXD-PIN onboard *Suzaku* has a far higher sensitivity to weak short bursts, as long as the source is inside its tightly

Table 1. List of detected short burst events.

ID	Time at burst peak (UTC)	T_{90} (ms)	N_{bst}^a	N_{T90}^b	1-s rate ^b	Model	Photon index	Flux ^c	Fluence ^c	χ_v^b (p-value)
1	2009-01-28T21:48:24.8	1851.4	9	(72, 26, 29)	(37, 15, 25)	PL	$1.65^{+0.16}_{-0.13}$	$0.5^{+0.1}_{-0.1}$	$9.0^{+1.1}_{-2.4}$	1.09(0.36)
2	2009-01-29T02:36:02.2	46.9	9	(16, 9, 4)	(26, 10, 25)	PL	$1.34^{+0.13}_{-0.12}$	$6.0^{+1.0}_{-1.6}$	$2.8^{+0.5}_{-0.7}$	0.81(0.60)
3	2009-01-29T03:06:21.3	148.4	5	(9, 4, 7)	(20, 6, 14)	PL	$1.07^{+0.29}_{-0.25}$	$1.3^{+0.3}_{-0.7}$	$1.9^{+0.5}_{-1.1}$	0.75(0.69)
4	2009-01-29T08:09:06.6	226.5	4	(17, 8, 10)	(21, 10, 21)	PL	$1.24^{+0.12}_{-0.12}$	$1.5^{+0.5}_{-0.4}$	$3.4^{+1.2}_{-0.9}$	1.19(0.31)
5	2009-01-29T08:53:23.4	78.1	5	(8, 5, 4)	(12, 9, 14)	PL	$1.18^{+0.19}_{-0.17}$	$2.4^{+0.5}_{-1.1}$	$1.9^{+0.4}_{-0.8}$	0.44(0.82)
6	2009-01-29T09:17:10.4	656.2	256	(2029, 219, 59)	(2107, 282, 93)	PL	—	—	—	—
7	2009-01-29T11:19:27.4	265.6	139	(127, 131, 84)	(155, 143, 101)	CutPL	$0.12^{+0.13}_{-0.14}$	$28.1^{+0.7}_{-3.4}$	$74.6^{+1.9}_{-9.1}$	0.82(0.74)
8	2009-01-29T12:16:56.4	390.6	19	(44, 23, 15)	(56, 28, 26)	PL	$1.49^{+0.08}_{-0.07}$	$1.8^{+0.4}_{-0.4}$	$7.1^{+1.4}_{-1.5}$	1.46(0.15)
9	2009-01-29T12:17:36.5	54.7	11	(19, 11, 10)	(34, 16, 32)	PL	$0.91^{+0.13}_{-0.13}$	$15.0^{+1.9}_{-4.3}$	$8.2^{+1.0}_{-2.3}$	0.28(0.95)
10	2009-01-29T12:58:41.1	78.1	44	(—, 38, 29)	(—, 47, 41)	PL	—	—	—	—
11	2009-01-29T13:41:57.1	164.1	8	(21, 8, 11)	(37, 10, 20)	PL	$1.45^{+0.14}_{-0.12}$	$2.5^{+0.5}_{-0.6}$	$4.1^{+0.8}_{-0.9}$	0.85(0.55)
12	2009-01-29T13:43:27.9	210.9	7	(7, 9, 13)	(13, 10, 26)	CutPL	$-0.38^{+0.39}_{-0.55}$	$4.0^{+0.8}_{-0.7}$	$8.4^{+1.7}_{-1.4}$	0.53(0.78)
13	2009-01-29T13:46:37.4	328.1	13	(97, 20, 19)	(113, 27, 26)	CutPL	$1.11^{+0.17}_{-0.18}$	$4.3^{+0.2}_{-1.3}$	$14.0^{+0.7}_{-4.3}$	0.87(0.56)
14	2009-01-29T13:50:38.2	835.9	60	(156, 62, 82)	(187, 67, 89)	CutPL	$0.83^{+0.09}_{-0.09}$	$5.5^{+0.3}_{-0.8}$	$45.9^{+2.5}_{-6.4}$	1.10(0.34)
15	2009-01-29T15:40:45.1	109.4	15	(35, 14, 14)	(44, 16, 24)	PL	$1.48^{+0.09}_{-0.08}$	$4.8^{+0.7}_{-0.9}$	$5.3^{+0.7}_{-1.0}$	1.23(0.26)
16	2009-01-29T16:51:40.5	265.6	90	(97, 85, 75)	(148, 96, 98)	CutPL	$0.28^{+0.12}_{-0.12}$	$21.1^{+0.9}_{-2.9}$	$56.1^{+2.4}_{-7.8}$	0.54(0.97)
17	2009-01-29T16:59:58.8	109.4	6	(19, 6, 5)	(24, 8, 19)	PL	$1.39^{+0.17}_{-0.15}$	$2.5^{+0.7}_{-1.1}$	$2.9^{+0.8}_{-1.2}$	0.78(0.60)
18	2009-01-29T18:42:12.6	54.7	5	(17, 6, 7)	(25, 8, 23)	PL	$1.38^{+0.19}_{-0.16}$	$6.5^{+1.6}_{-1.7}$	$3.6^{+0.9}_{-1.0}$	0.27(0.97)

^aAn event train of length N_{bst} is defined in Section 2.2.

^b N_{T90} and 1-s rate around the burst are shown in a form of (XIS0, PIN, GSO). The former is a burst photon count during T_{90} defined in Section 3.1. The latter is extracted from 1-s binned light curves in Fig. 2.

^cFlux is shown in units of $10^{-8} \text{ erg s}^{-1} \text{ cm}^{-2}$ and fluence is in $10^{-9} \text{ erg cm}^{-2}$, both in the 10–70 keV band.

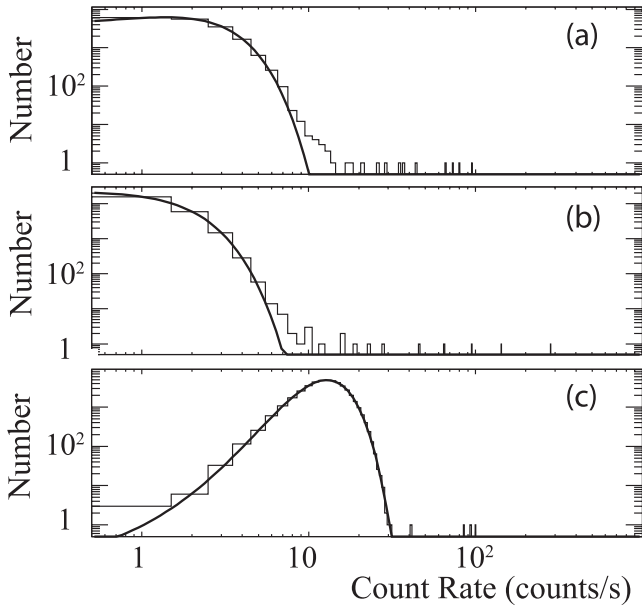


Figure 4. Distributions of 1-s count rates for the (a) XIS1+3, (b) HXD-PIN and (c) HXD-GSO data. The best-fitting Poisson distributions are also shown.

collimated field of view. Therefore, we utilize the above *Suzaku* data set for the following analyses.

3 ANALYSIS

3.1 Detected bursts

Fig. 5 shows the XIS, HXD-PIN, and HXD-GSO light curves of the bursts described in Section 2.2. Table 1 also gives their basic properties. The bursts are clearly detected by HXD-PIN and XIS0, and a considerable fraction of them are detected by HXD-GSO as well. Because of the burst option, the coverage of these bursts with XIS1 and XIS3 (not shown in Fig. 5) is highly incomplete. However, this does not hamper our study, because we analyse below the XIS0 and HXD data of these bursts. We exclude Burst-6, presumably the strongest burst, because some of the HXD data were lost as a result of the saturation of the data transfer. Likewise, Burst-10 is discarded, because it fell outside the good time interval (GTI) of the XIS. Thus, hereafter we analyse the remaining 16 short bursts. These are statistically significant with chance probabilities $\lesssim 10^{-5}$ when combining the 1-s data of XIS, HXD-PIN and HXD-GSO together (see Appendix B; the 1-s rates are also shown in Table 1), and they are free from data losses because of dead-time or pile-ups (Appendix C).

The burst peaks in Table 1 are defined as the times of the maximum count rates of HXD-PIN, which have higher signal-to-noise ratios than the others. As can be seen in Fig. 5, these peaks can be determined with a typical uncertainty of a few bins, or $\lesssim 50$ ms. Taking a closer look at individual light curves in Fig. 5, some burst photons apparently appear outside the duration of N_{bst} (Table 1) defined in Section 2.2. Thus, using the XIS0 (2–10 keV) and HXD-PIN (10–70 keV) data co-added together, we have manually defined tentative burst durations to cover all possible burst X-ray photons. Within the above durations, we have further calculated the time period, T_{90} , starting when 5 per cent of the XIS0+PIN photons have been detected, and ending when 95 per cent have been

observed. As shown in Fig. 6 (see also Table 1), the T_{90} values range from ~ 47 ms to 1.9 s, with an average of 321 ms. This value is close to the mean values derived in recent studies of the same object, $T_{90} = 258$ ms (van der Horst et al. 2012) and 305 ms (Scholz & Kaspi 2011). Here, the disagreement might have arisen because these authors used different sets of short bursts, with different fluences and different energy ranges. Fig. 7 represents distributions of burst photon counts N_{T90} detected during T_{90} . Thus, N_{T90} of the 10–70 keV PIN data are distributed from ~ 5 to ~ 130 . Although N_{T90} is sometimes slightly different from N_{bst} by up to ~ 50 per cent, the difference is negligible in the following analyses.

For spectral analyses of the individual bursts, the XIS0 and the HXD events accumulated over T_{90} were utilized as source spectra. The background of XIS0 was extracted using actual events on the CCD chip far away from the source position. The HXD-PIN background was not subtracted, because the average background rate (~ 0.8 Hz in 10–70 keV) implies at most \sim one photon in T_{90} . However, for the HXD-GSO analyses, we have produced the background spectra from the simulated GSO events (Fukazawa et al. 2009) during a 20-s period around the corresponding burst. We then subtracted them, after scaling to the duration of T_{90} . The GSO background typically contains \sim eight counts per burst, which amounts to ~ 30 per cent of the signal counts. Although we did not produce background from the actual GSO data taken before/after the bursts, in order to avoid possible contamination of the persistent or burst emission from the source, this alternative method gives consistent results. We have employed standard response files (epoch 5) for the HXD, while we have used the response matrix files (RMFs) and auxiliary response files (ARFs) for XIS0, produced as in Section 2.1.

The average fluxes and fluences of these bursts were estimated using a single PL model, with a column density of the photoabsorption fixed at $N_{\text{H}} = 3.2 \times 10^{22} \text{ cm}^{-2}$, following Paper I. Table 1 lists the resultant photon indices and the 10–70 keV X-ray fluxes. In some bursts, this PL model did not give an acceptable fit, mainly because of a high-energy signal deficiency. For such bursts, we alternatively utilized a cut-off power-law model (CutPL) with the same fixed photoabsorption. The 10–70 keV fluences integrated over T_{90} are also shown in Table 1. As one of the characteristics of the present burst sample, Fig. 8 shows hardness ratios of the burst photons detected by the HXD to those by the XIS, as a function of their fluences. The fluences are distributed in the range of $\sim 10^{-9}$ – $10^{-7} \text{ erg cm}^{-2}$, and their hardness ratios ranges from ~ 0.4 to ~ 3 . Although a hardening trend towards weaker bursts was reported from SGRs (Göğüş et al. 2001), and a softening trend was reported from AXPs (Gavril, Kaspi & Woods 2004), the present sample shown in Fig. 8 does not show any significant corrections between the hardness and fluence.

Among the above 16 short bursts, for our detailed spectral analyses, we selected three outstandingly bright bursts, Burst-7, Burst-14 and Burst-16, which all satisfy $N_{\text{bst}} \geq 60$ and show fluences above $2 \times 10^{-8} \text{ erg s}^{-1}$ (Fig. 8). Although these are the brightest bursts among the present sample (except for Burst-6, which was discarded), they are still weaker compared to most of the bursts used in previous studies, for which the fluences are typically $\sim 10^{-8}$ – $10^{-4} \text{ erg cm}^{-2}$. Below, we apply several spectral modellings to these bursts in the ~ 1 –300 keV energy range. For all models, the column density for photoabsorption is fixed at $N_{\text{H}} = 3.2 \times 10^{22} \text{ cm}^{-2}$ as before, unless otherwise noted. The normalization factor of XIS0 to the HXD was fixed at 1.08, based on the correction as described in Section 6.2, although allowing it to float has an insignificant effect on the following results.

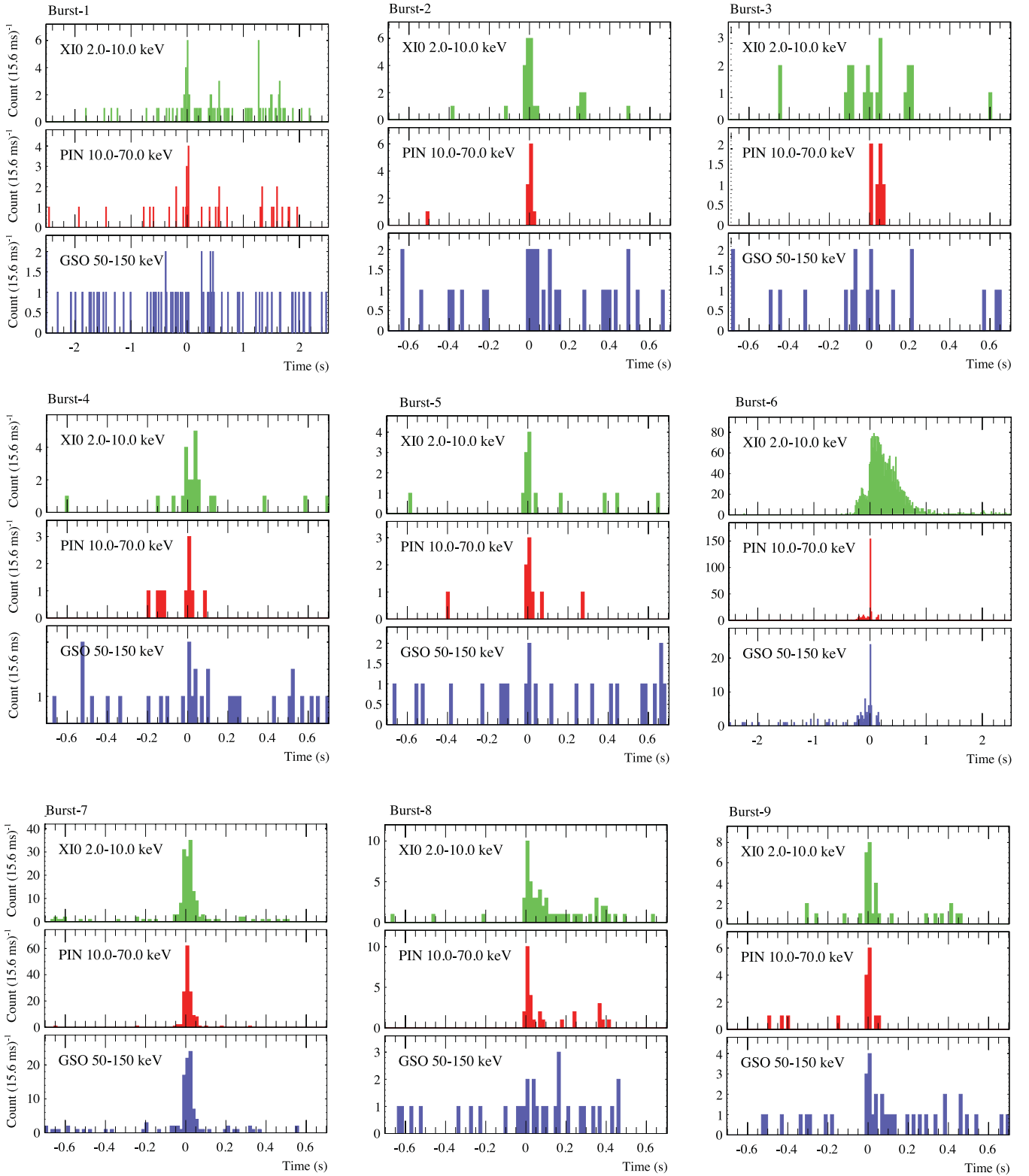


Figure 5. Light curves of the individual short burst events detected by the present *Suzaku* observation. From top to bottom, the panels refer to those obtained with XIS0, HXD-PIN and HXD-GSO in 2–10, 10–70 and 50–150 keV, respectively. The time bin is 15.6 ms.

The single PL model with the fixed N_H gave acceptable fits to none of the three bursts, with reduced χ^2_ν values of 4.92, 2.83 and 3.89 for Burst-7, Burst-14 and Burst-16, respectively. Even if we make N_H free, the fits are still unacceptable ($\chi^2_\nu \sim 2$). Discrepancies

of these fits originate from model excess at the lowest and highest spectral ends. An optically thin bremsstrahlung model is not successful either ($\chi^2_\nu > 2$). Then, we fitted these spectral data using the CutPL model, and obtained acceptable fits, as summarized in

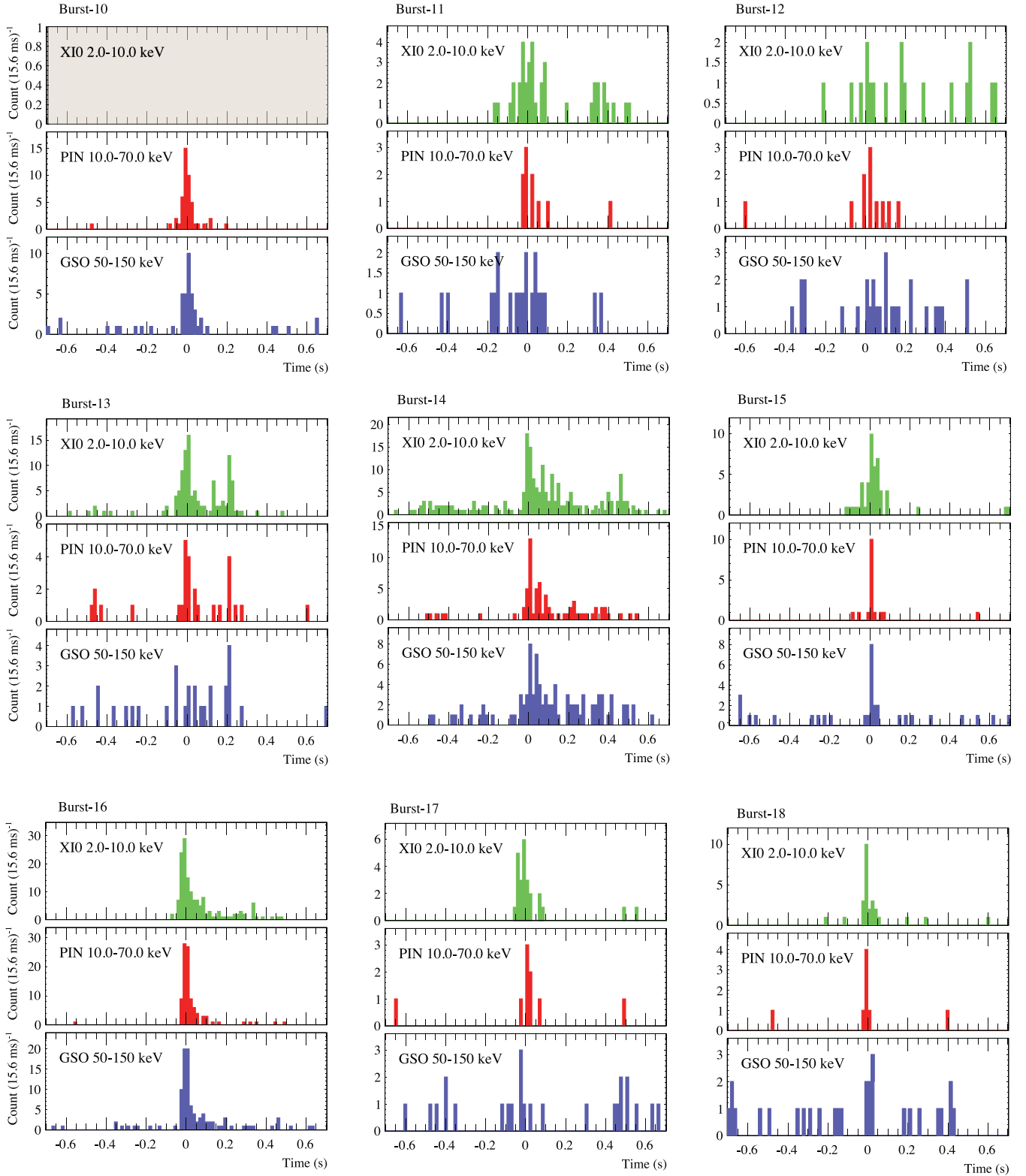


Figure 5 – continued

Table 2 and in Fig. 9. The fits yielded a photon index of $\Gamma \sim 0.1\text{--}0.8$ and a cut-off energy of $E_{\text{cut}} \sim 27\text{--}66$ keV. As alternative models, we utilized a two-blackbody (2BB) model. As shown in Table 2, it was also successful on the three bursts, and yielded the lower and higher temperatures of $\sim 3\text{--}5$ keV and $\sim 18\text{--}20$ keV, respectively.

In Figs 9(a4), (b4) and (c4), the above two best-fitting spectral models (the CutPL and 2BB) are compared in νF_ν forms. These give relatively similar spectral shapes, except in the higher-energy range above ~ 100 keV, where the models become unconstrained. In both models, spectral peaks appear in the HXD-PIN band

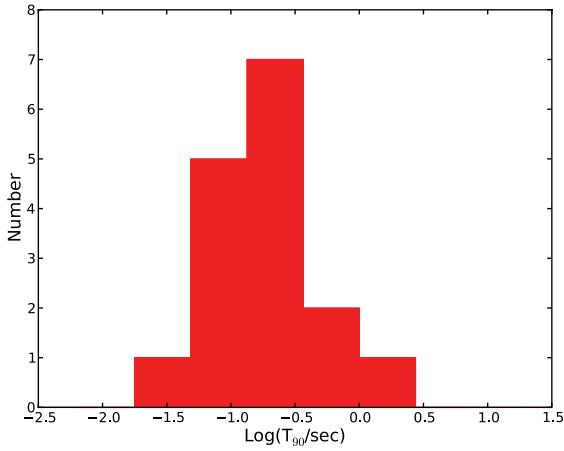


Figure 6. Distribution of T_{90} for the 16 bursts determined from the 10–70 keV HXD-PIN data.

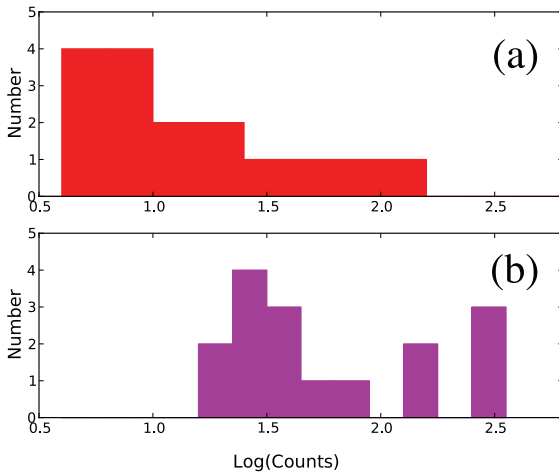


Figure 7. (a) Distribution of burst counts recorded over T_{90} in the 10–70 keV HXD-PIN data. (b) Same as panel (a), but for the total counts summed over the 2–10 keV XIS, 10–70 keV HXD-PIN and 50–150 keV HXD-GSO data.

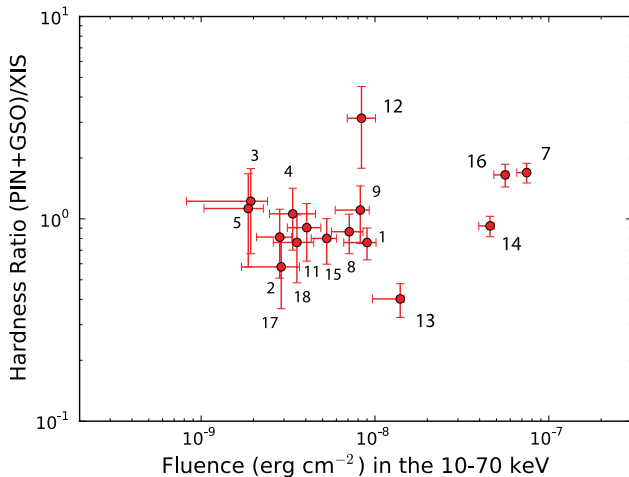


Figure 8. Hardness ratios of the detected X-ray photons N_{T90} during T_{90} calculated as (PIN+GSO)/XIS0, as a function of the 10–70 keV fluence. Numbers in the figure indicate the corresponding burst ID.

(~ 50 – 100 keV). Employing the CutPL model conventionally, the absorption-corrected 0.2–300 keV fluences of Burst-7, Burst-14 and Burst-16 are obtained as 1.1×10^{-7} , 9.3×10^{-8} and 8.7×10^{-8} erg cm^{-2} , respectively. The fluence becomes ~ 4 – 8×10^{-8} erg cm^{-2} if calculated in the 10–70 keV band.

In Fig. 10(a), we compare the spectrum of the brightest Burst-7 with the persistent X-ray spectrum recorded during the same observation (Paper I). While the persistent spectrum is apparently composed of two components, the burst spectrum is more curved, without apparent evidence for such a two-component nature.

3.2 Weak short bursts

As shown in Fig. 8, the remaining 13 short bursts have considerably lower 10–70 keV fluences than the three studied above, distributed below 2×10^{-8} erg cm^{-2} . They have poorer statistics, and also tend to show similar hardness ratios around ~ 1.0 . Therefore, we have stacked their spectra together for a detailed analysis, with an accumulated total exposure of 3.7 s. In order to justify the stacking procedure, we have taken the spectral ratios of each burst to the stacked one, and we have found that the ratios can be fitted, in each case, successfully by a constant with a reduced χ^2 of $\lesssim 1.0$. Therefore, we conclude that the 13 bursts have consistent spectral shapes, and hence the stacking procedure can be justified. The derived 13 constant ratios are distributed from 0.55 to 3.3, with the average and standard deviations of 1.56 and 1.05, respectively. This distribution, ranging by a factor of 6, agrees with that of the fluence shown in Fig. 8. In this analysis, we have used the same responses as those of the brighter three short bursts, and in the same way as the previous analyses, the background was subtracted from the XIS0 and HXD-GSO data.

Fig. 11 shows the stacked light curve of these weaker short bursts, accumulated with reference to their peak times. Thus, the burst emission is highly significant even in the HXD-GSO band. Fig. 12(a) shows the raw spectrum of this cumulative weak-burst data after the background subtraction. Its average 10–70 keV flux is an order of magnitude lower than those of the three brightest bursts. The HXD-GSO background becomes comparable to the signal level around ~ 130 keV, and we can claim the HXD-GSO detection at least up to 150 keV at 2.8σ .

As summarized in Table 3, a PL model with fixed N_{H} failed to give an acceptable fit ($\chi^2_{\nu} \sim 2.1$; Fig. 12b), while a PL model with free N_{H} was more successful ($\chi^2_{\nu} \sim 1.3$), yielding $\Gamma = 1.57 \pm 0.04$ and $N_{\text{H}} = 5.4^{+0.8}_{-0.5} \times 10^{22}$ cm^{-2} (Fig. 12c). In order to further improve the fit, especially in higher-energy range, we again tried the CutPL and 2BB fits with the same column density fixed at $N_{\text{H}} = 3.2 \times 10^{22}$ cm^{-2} . As summarized in Table 3 and shown in Fig. 12(d), the CutPL model gave an acceptable fit ($\chi^2_{\nu} \sim 0.8$) with $\Gamma = 1.03 \pm 0.07$ and $E_{\text{cut}} = 62.9^{+14.5}_{-10.8}$ keV, implying a mild spectral curvature. Because Γ and E_{cut} couple with each other, in Fig. 13, we show the fit confidence contours on the Γ – E_{cut} plane. In contrast to the successful CutPL model, the more convex 2BB model, which was successful on the brightest three bursts (Section 3.1), became much less successful ($\chi^2_{\nu} \sim 1.6$; Fig. 12e). Thus, the weaker bursts are considered to have a flatter 10–70 keV HXD-PIN spectrum than the brightest bursts, particularly Burst-7 and Burst-16.

To make the above spectral difference clearer, we added the stacked weak bursts to Fig. 10(a) in νF_{ν} form, where we employed the CutPL model for deconvolution in the same way as Burst-7. The weaker bursts are \sim two orders of magnitude brighter than the persistent emission, and \sim one order of magnitude fainter than Burst-7. As depicted by this plot, the cumulative burst shows a hard

Table 2. Spectral parameters of the three brightest short bursts.

Spectral model	Parameter	Burst-7	Burst-14	Burst-16
wabs ^b	Time (2011-01-29)	11:19:27.4	13:50:38.2	16:51:40.5
	T_{90} (s)	0.2656	0.8359	0.2656
	Fluence ^a (10^{-8} erg cm ⁻²)	$7.46^{+0.48}_{-0.82}$	$4.60^{+0.25}_{-0.67}$	$5.60^{+0.24}_{-0.72}$
	N_H (10^{22} cm ⁻²)	(3.2 fix)	(3.2 fix)	(3.2 fix)
CutPL	Photon index Γ	$0.12^{+0.13}_{-0.14}$	0.83 ± 0.09	0.28 ± 0.12
	Cut-off energy E_{cut} (keV)	$26.9^{+4.4}_{-3.8}$	$65.7^{+16.7}_{-12.3}$	$31.9^{+4.8}_{-4.1}$
	PIN flux ^c (10^{-7} erg s ⁻¹ cm ⁻²)	$2.81^{+0.18}_{-0.31}$	$0.55^{+0.03}_{-0.08}$	$2.11^{+0.09}_{-0.27}$
	Total flux ^d (10^{-7} erg s ⁻¹ cm ⁻²)	$4.01^{+0.14}_{-0.51}$	$1.08^{+0.07}_{-0.18}$	$3.21^{+0.11}_{-0.56}$
	Fit goodness χ^2_ν (ν)	0.82 (28)	1.10 (20)	0.54 (25)
	Figure	Figs 9(a1), (a2), (a5)	Figs 9(b1), (b2), (b5)	Figs 9(c1), (c2), (c5)
2BB	kT_{Low} (keV)	$5.28^{+0.43}_{-0.42}$	$2.58^{+0.47}_{-0.34}$	3.97 ± 0.41
	R_{Low} (km)	$1.78^{+0.20}_{-0.18}$	$2.88^{+1.51}_{-1.02}$	$2.18^{+0.31}_{-0.27}$
	kT_{High} (keV)	20.5 ± 2.1	$20.9^{+2.7}_{-2.5}$	$17.5^{+1.8}_{-1.7}$
	R_{High} (km)	$0.142^{+0.038}_{-0.028}$	$0.0766^{+0.0216}_{-0.0165}$	$0.191^{+0.047}_{-0.0381}$
	PIN flux ^c (10^{-7} erg s ⁻¹ cm ⁻²)	$2.54^{+0.12}_{-0.35}$	$0.45^{+0.01}_{-0.12}$	$1.91^{+0.12}_{-0.29}$
	Total flux ^d (10^{-7} erg s ⁻¹ cm ⁻²)	$4.05^{+0.13}_{-0.70}$	0.98 ± 0.02	$3.05^{+0.12}_{-0.45}$
	Fit goodness χ^2_ν (ν)	0.62 (27)	0.79 (18)	0.58 (24)
	Figure	Figs 9(a3), (a5)	Figs 9(b3), (b5)	Figs 9(c3), (c5)
2BB + PL	kT_{Low} (keV)	$5.85^{+0.67}_{-0.57}$	$2.90^{+0.30}_{-0.28}$	$4.35^{+0.63}_{-0.54}$
	R_{Low} (km)	$1.45^{+0.24}_{-0.22}$	$1.99^{+0.37}_{-0.33}$	$0.565^{+0.050}_{-0.049}$
	kT_{High} (keV)	$20.2^{+2.5}_{-2.3}$	$20.9^{+2.9}_{-2.6}$	$17.1^{+1.9}_{-1.8}$
	R_{High} (km)	$0.139^{+0.042}_{-0.033}$	$0.0730^{+0.0219}_{-0.0167}$	$0.191^{+0.052}_{-0.041}$
	Γ_{bst}	1.54 (fix)	1.54 (fix)	1.54 (fix)
	PL flux ^d (10^{-7} erg s ⁻¹ cm ⁻²)	$0.410^{+0.190}_{-0.195}$	$0.140^{+0.092}_{-0.093}$	$0.339^{+0.196}_{-0.200}$
	Fit goodness χ^2_ν (ν)	0.48 (26)	0.68 (18)	0.49(23)
	Figure	Fig. 14(a)	Fig. 14(b)	Fig. 14(c)

^aFluences are estimated using the CutPL model in the 10–70 keV range with T_{90} .

^bThe interstellar absorption (wabs) is multiplied to each model.

^cAbsorbed X-ray fluxes in the 10–70 keV energy range at its average value.

^dAbsorbed X-ray fluxes in the 1–300 keV energy range at its average value.

X-ray spectrum, which is less curved than that of Burst-7 and is similar to that of the persistent X-rays. In fact, the value of $\Gamma_{\text{bst}} = 1.57 \pm 0.04$, obtained above by the PL fit with free N_H , is consistent with $\Gamma_{\text{per}} = 1.54^{+0.03}_{-0.04}$ of the persistent hard component (Table 3). Although the CutPL model gives a much harder photon index, $\Gamma_{\text{bst}} = 1.03 \pm 0.07$, the slope is still similar, if we consider the effect of the cut-off around ~ 63 keV.

In order to more directly compare these νF_ν spectra, we divided the stacked weak-burst spectrum by that of the persistent emission. As shown in Fig. 10(b), the resulting ratios remain constant at ~ 170 over the ~ 8 –200 keV energy range. The remaining difference in the ratio below ~ 8 keV in Fig. 10(b) is thought to originate mainly from the presence of the soft BB component. Thus, we recalculated the same ratio in Fig. 10(c) after eliminating the soft BB component from the persistent spectrum. Thus, the ratio became much flatter, even at energies below ~ 10 keV, suggesting that the weak-burst spectrum is similar in shape to the hard X-ray component in the persistent emission.

Finally, in order to examine our weak-burst sample for its homogeneity, we subdivided the 13 bursts randomly into two subsets, under the constraint that they should be comparable, to within 10 per cent in the summed signal photon counts (XISO, PIN and GSO summed). From the two subsets, we then produced two stacked spectra instead of one, and we analysed them in the same manner as before. The pair of CutPL parameters obtained in this way are indicated in Fig. 13 by a pair of data points with the same symbol.

By trying six different partitions, we have confirmed that the two subsets always give, within errors, consistent model parameters, which, in turn, are also consistent with those derived from the entire sample (indicated by contours). Therefore, the present sample can be regarded, within errors, as homogeneous.

3.3 Fitting by thermal/non-thermal components

Let us further examine the suggestion of Fig. 10 that the burst emission has the same spectral components as the persistent X-ray emission. In particular, the good similarity above ~ 8 keV points to possible presence of the hard PL component in the stacked weak-burst spectrum, as in the persistent emission spectra. The short bursts from the transient magnetar SGR 0501+4516 have already been examined for such a possibility with an affirmative answer (Nakagawa et al. 2011).

In order to assess the above consideration, we reanalysed the stacked weak-burst spectrum, by adding, to the 2BB model, a hard PL with its slope fixed at $\Gamma_{\text{per}} = 1.54$, as specified by the persistent emission (Paper I). The inclusion of the hard PL has made the 2BB fit acceptable, as summarized in Fig. 12(f) and Table 3. The additional PL contributes to the total 1–300 keV flux by 52 per cent, and is statistically significant, because the achieved fit improvement, $\Delta\chi^2 = -27.1$, implies an F -test chance probability of 2.4×10^{-7} . Even though an acceptable fit with a comparable goodness had already been obtained with the CutPL model, we consider the

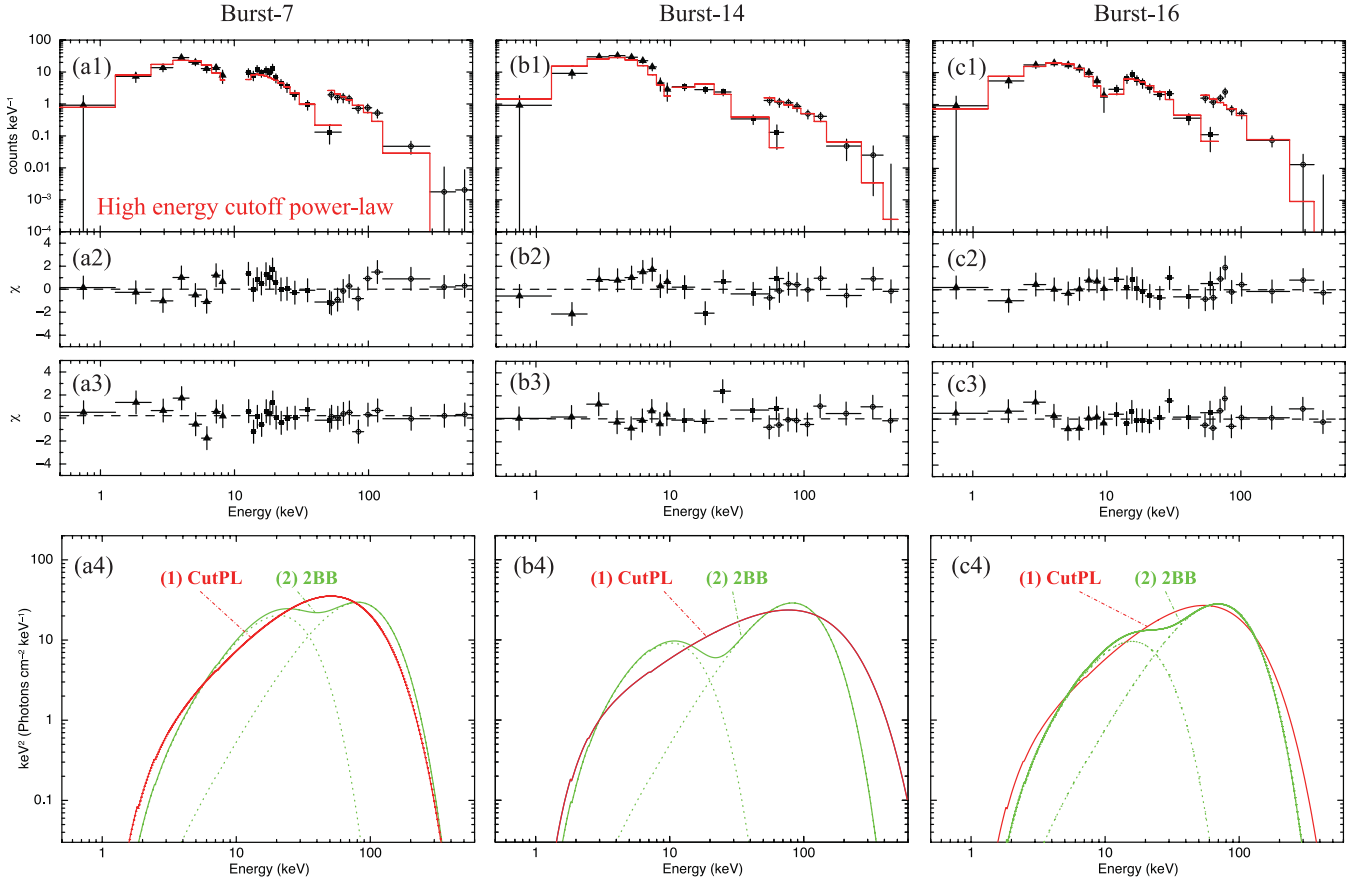


Figure 9. X-ray spectra of the three brightest bursts in our sample: Burst-7 (panels a1–a5), Burst-14 (panels b1–b5) and Burst-16 (panels c1–c5). Raw count spectra with XIS0, HXD-PIN and HXD-GSO are shown in panels (1) with the best-fitting CutPL model, and the corresponding residuals are shown in panels (2). Panels (3) are residuals when the data are fitted by the 2BB model. Panels (4) are comparisons among the inferred best-fitting CutPL (red) and 2BB (green) models. The spectra are shown after being multiplied by individual T_{90} values. The XIS0 and HXD-GSO backgrounds were subtracted, as described in Section 3.1.

2BB+PL modelling more appropriate, for the following two reasons. (i) This modelling has successfully explained the spectra of weak short bursts from SGR 0501+4516 (Nakagawa et al. 2011). (ii) The 2BB model has been regarded as a standard representation of the short-burst spectra of a fair number of magnetars (Nakagawa et al. 2007, and references therein), so our final model should also be based on this, rather than the CutPL model, which in the present case is quite conventional.

Now that evidence for the PL component has been obtained in the stacked weak-burst spectrum, it would be a natural step to examine the brighter bursts, Burst-7, Burst-14 and Burst-16, for the same possibility, even though their spectra have already been represented successfully by the 2BB model. This is because the distinction between the brighter and fainter bursts in the present observation is purely technical, without any particular reason to consider that the two groups have a distinct nature. Then, to the 2BB model describing the three bright bursts, we added the hard PL with Γ_{bst} fixed at the same value. This improved the fit to Burst-7, Burst-14 and Burst-16, by $\Delta\chi = -4.3$, -2.0 and -2.8 , respectively, giving F -test probabilities of 0.60, 7.4 and 2.4 per cent, respectively. Thus, the hard PL component is likely to contribute to Burst-7, at least. The best-fitting spectra are shown in Fig. 14 in νF_ν forms, with the derived parameters in Table 2. The BB temperatures did not change within errors from those obtained in the previous pure 2BB modelling (Section 3.1), while the hard PL component was found

to contribute to the total 1–300 keV fluxes of Burst-7, Burst-14 and Burst-16, by 10, 14 and 19 per cent, respectively.

4 DISCUSSION

4.1 Spectral comparison among different emissions

During the 33.5 ks of effective exposure with the HXD on to 1E 1547.0–5408 during its activity in 2009 January, we detected 18 short bursts with their fluence S above $S_{\text{min}} \sim 2 \times 10^{-9}$ erg cm $^{-2}$, and we have analysed 16 of them. Even the strongest three of the 16 bursts, with a 10–70 keV fluence of $S = 4\text{--}8 \times 10^{-8}$ erg cm $^{-2}$ (or $\sim 1 \times 10^{-7}$ erg cm $^{-2}$ in 1–300 keV), are still weaker than most of the previously reported bursts from magnetars, in general, which typically have $S \gtrsim 10^{-7}$ erg cm $^{-2}$. For example, the burst forest of 1E 1547.0–5408, observed on 2009 January 22 with *Swift*, *INTEGRAL*, *Suzaku* and *Fermi*, was composed of events with $S \gtrsim 2 \times 10^{-6}$ erg s $^{-1}$ up to 2.5×10^{-4} erg cm $^{-2}$ (Mereghetti et al. 2009). Therefore, the present *Suzaku* results, together with those of Nakagawa et al. (2011) for SGR 0501+4516, provide valuable information on the wide-band spectra of weak short bursts. For reference, the present sample defines a burst frequency of 5.4×10^{-4} burst s $^{-1}$ in the range of $S \gtrsim S_{\text{min}}$.

So far, the wide-band spectra of many energetic ($S > 10^{-7}$ erg s $^{-1}$) short bursts from magnetars have been explained successfully by

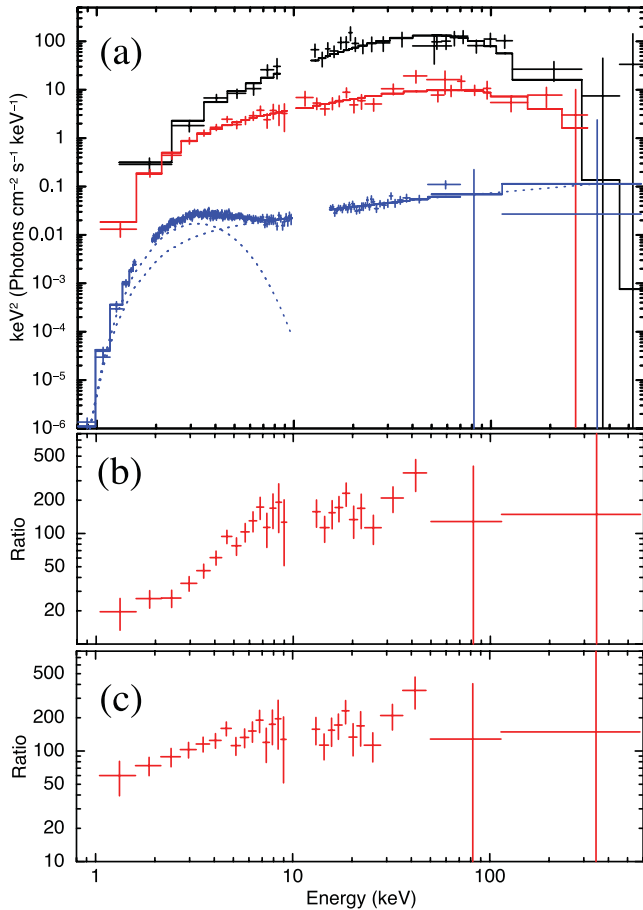


Figure 10. (a) Comparison of X-ray spectra of 1E 1547.0–5408 in νF_ν forms. Top (black), middle (red) and bottom (blue) spectra represent Burst-7, the accumulated weak short bursts and the persistent emission from Paper I, respectively. The CutPL model was employed to deconvolve Burst-7 (Table 2) and the accumulated weak-burst spectra (Table 3), while a PL plus a BB were used for the persistent emission. The column density of the photoabsorption was fixed at $3.2 \times 10^{22} \text{ cm}^{-2}$ in all cases. (b) The ratio between the red and blue spectra in panel (a). (c) Same as panel (b), but after eliminating the BB component from the persistent emission.

the 2BB model. These include numerous bursts from SGR 1806–20 and SGR 1900+14 (Nakagawa et al. 2007; Israel et al. 2008), as well as the strongest *Suzaku* burst from SGR 0501+4516 (Enoto et al. 2009; Nakagawa et al. 2011). At the same time, the 2BB model can generally reproduce the soft X-ray component, which is ubiquitously seen at energies of $\lesssim 10$ keV for the wide-band persistent spectra from magnetars (Mereghetti 2008), including 1E 1547.0–5408 itself (Paper I). These 2BB fits to the two different forms of magnetar emission reveal an interesting common scaling, $T_{\text{Low}}/T_{\text{High}} \sim 0.4$ (Nakagawa et al. 2009), where T_{Low} and T_{High} denote the lower and higher 2BB temperatures, respectively. These results reinforce the possibility that the persistent emission is composed of numerous micro short bursts (see Section 1; Thompson & Duncan 1996; Lyutikov 2003; Nakagawa 2007). Because the 2BB modelling is considered to have some physical meaning beyond mere convention, here we construct our discussion based on the 2BB modelling rather than on the CutPL model, which is rather empirical.

The three brightest bursts in our present sample, particularly the brighter two bursts, Burst-7 and Burst-16, exhibit upward convex

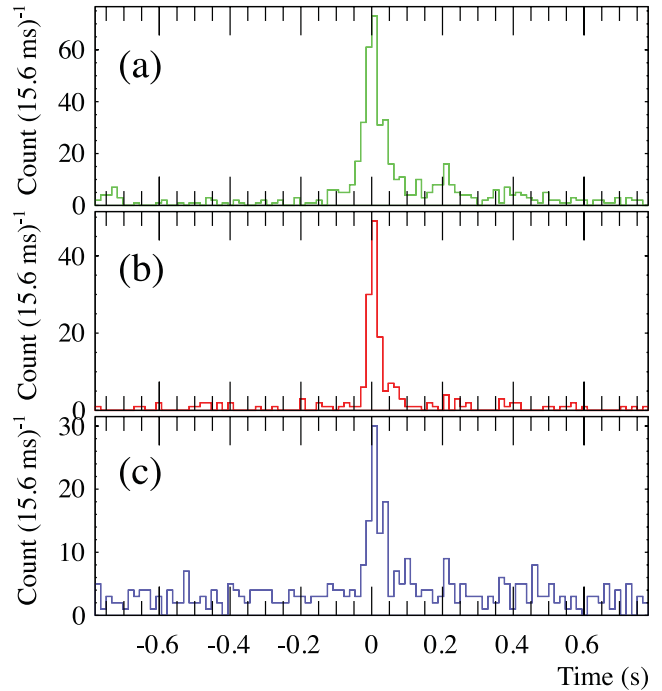


Figure 11. Light curves obtained by stacking the 13 weaker short bursts, with XIS0 (a), HXD-PIN (b) and HXD-GSO (c) in the 2–10, 10–70 and 50–150 keV bands, respectively.

spectral shapes, which have been successfully described by the 2BB model over an extremely wide energy band of ~ 1 to ~ 300 keV (Section 3.1). Importantly, the values of T_{Low} and T_{High} derived from these bursts (except for Burst-14, possibly) obey the above scaling relation. In contrast, the stacked weaker bursts have a less convex shape (Fig. 10), and do not accept the simple 2BB modelling. This is understandable if we presume that the spectra of weaker bursts are contributed by the hard component with a PL photon index $\Gamma \sim 1$, which is generally observed in the persistent emission of magnetars (Kuiper et al. 2006; Enoto et al. 2010c). The weak bursts from SGR 0501+4516, when stacked together, actually exhibit a hard-tail feature (Nakagawa et al. 2011). In fact, Figs 10(b) and (c) provide supporting evidence for this possibility, where the ratios become flatter above ~ 8 keV. Accordingly, we have added a hard PL component to the 2BB model in Section 3.3, fixing Γ at the same value as obtained from the persistent emission. We have obtained a fully acceptable spectral fit. Thus, the hard component is significantly present in the stacked weak-burst spectrum, as long as the 2BB model is chosen as the starting point of the analysis. As a further justification of this 2BB+PL modelling, the stacked spectrum yields $T_{\text{High}}/T_{\text{Low}} = 4.9 \pm 1.1$ (from Table 3) in agreement with the ‘canonical’ ratio, which was 7.3 ± 0.5 before properly including the PL component. As argued by Nakagawa et al. (2011), these strengthen the similarity between the burst and persistent emissions. Israel et al. (2008) have reported that weaker bursts tend to show harder spectra in terms of the 2BB analysis, which can be understood if we consider the possible contributions of the same PL component to their weaker bursts.

The above results have led us to a natural question about brighter short bursts, whose spectra generally lack a PL component: is this an intrinsic effect because of, for example, some changes in the emission mechanism, or is this an artefact caused by their higher 2BB temperatures, which mask any PL emission? With this in mind,

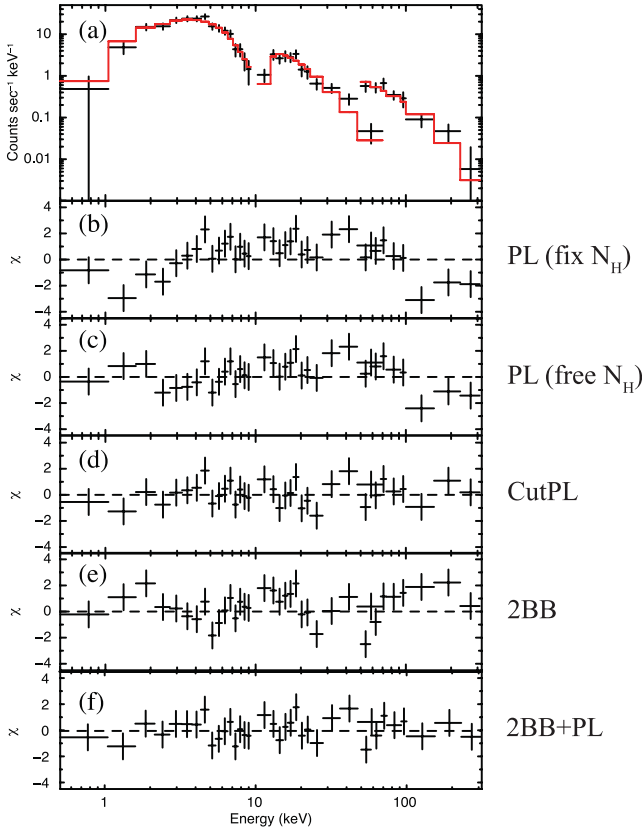


Figure 12. (a) Background-subtracted and response-inclusive spectra of the stacked weak bursts from 1E 1547.0–5408, compared with the best-fitting CutPL model (Table 3). Panels (b)–(f) show residuals when using a PL model with the fixed column density, a PL with the column density left free, a CutPL model, a 2BB model and a 2BB+PL model, respectively.

we have examined (Section 3.3) the spectra of the three brighter *Suzaku* bursts, for a possible contribution from such a hard component. The presence of the PL component (on top of the 2BB model) was suggested in Burst-7 at a relatively high confidence (>97 per cent) level. The results are presented in Fig. 15 on the thermal (2BB) versus non-thermal (PL) luminosity plane, in comparison with the weak-burst and persistent spectra. There, assuming a source distance of 4 kpc (Tiengo et al. 2010), the persistent X-ray emission (Paper I) is represented by a bolometric BB luminosity of $L_{BB} = 1.2 \times 10^{35}$ erg s⁻¹ and an absorption-corrected 1–300 keV PL luminosity of $L_{PL} = 6.9 \times 10^{35}$ erg s⁻¹. These sum up to give the total luminosity of $L_{per} = 8.1 \times 10^{35}$ erg s⁻¹. We also quote the results for SGR 0501+4516, taken from Nakagawa et al. (2011). Although it is still difficult at present to distinguish the two alternatives, the PL luminosity (if it is universally present in short bursts) appears to saturate at $\sim 10^{38}$ erg s⁻¹, so we prefer the former possibility.

On large scales, Fig. 15 reveals a clear positive correlation between the luminosities of the two emission components. Therefore, the soft (thermal) and hard (PL) components are considered to approximately keep their luminosity ratio over a very broad scale in flux or fluence. Similarly, Enoto et al. (2010c) have shown that the luminosity ratio between these two emission components, comprising persistent emission, is not much different between active magnetars and those in quiescence. These facts give further support to the microburst conjecture.

Table 3. Spectral parameters of the accumulated weaker short burst. All the quoted errors are at the 1σ level.

Burst emission		
	Summed exposure (s)	3.7
	Average fluence ^a (erg cm ⁻²)	$6.61^{+0.04}_{-2.04} \times 10^{-9}$
Spectral model	Parameter	Value
PL (N_H fixed)	N_H (10^{22} cm ⁻²)	3.2 (fix)
	Photon index Γ_{bst}	1.5
	Fit goodness χ^2_ν (ν)	2.05 (34)
PL	N_H (10^{22} cm ⁻²)	$5.4^{+0.8}_{-0.5}$
	Photon index Γ_{bst}	1.57 ± 0.04
	Flux ^a (10^{-8} erg s ⁻¹ cm ⁻²)	1.7 ± 0.1
	Fit goodness χ^2_ν (ν)	1.29 (33)
CutPL	N_H (10^{22} cm ⁻²)	3.2 (fix)
	Photon index Γ_{bst}	1.03 ± 0.07
	Cut-off energy E_{cut} (keV)	$62.9^{+14.5}_{-10.8}$
	Flux ^a (10^{-8} erg s ⁻¹ cm ⁻²)	$2.3^{+0.1}_{-0.2}$
	Fit goodness χ^2_ν (ν)	0.81 (33)
2BB	N_H (10^{22} cm ⁻²)	3.2 (fix)
	kT_{Low} (keV)	$1.68^{+0.17}_{-0.15}$
	R_{Low} (km)	$3.33^{+0.52}_{-0.46}$
	kT_{High} (keV)	$12.3^{+0.9}_{-0.8}$
	R_{High} (km)	$0.140^{+0.021}_{-0.018}$
	Flux ^a (10^{-8} erg s ⁻¹ cm ⁻²)	2.5 ± 0.2
	Fit goodness χ^2_ν (ν)	1.63 (32)
	Persistent emission ^b	
2BB + PL	N_H (10^{22} cm ⁻²)	3.2 (fix)
	kT_{Low} (keV)	$2.71^{+0.50}_{-0.48}$
	R_{Low} (km)	$1.16^{+0.41}_{-0.29}$
	kT_{High} (keV)	$13.3^{+2.0}_{-1.6}$
	R_{High} (km)	$0.0905^{+0.0283}_{-0.0255}$
	Γ_h	1.53 (fix)
BB + PL	PL flux ^a (10^{-8} erg s ⁻¹ cm ⁻²)	0.78 ± 0.13
	Fit goodness χ^2_ν (ν)	0.82 (31)
	N_H (10^{22} cm ⁻²)	3.2 ± 0.1
	kT (keV)	$0.65^{+0.02}_{-0.01}$
BB + PL	Γ_{per}	$1.54^{+0.03}_{-0.04}$
	Flux ^a (10^{-10} erg s ⁻¹ cm ⁻²)	$1.40^{+0.05}_{-0.07}$
	Fit goodness χ^2_ν (ν)	1.08 (278)

^a Average fluence is evaluated in the 10–70 keV band assuming the 2BB+PL model. Flux is estimated in the 10–70 keV band.

^b Values from Paper I. The quoted errors are converted to the 1σ level.

4.2 The log N –log S relation of short bursts

In order to examine the possibility that the persistent X-ray emission is composed of microburst events, it is inevitable that we should evaluate X-ray fluxes accumulated over resolved and unresolved burst events. Because the present short bursts, with $S \gtrsim S_{min} \sim 2 \times 10^{-9}$ erg cm⁻², were detected at a low burst frequency, 5×10^{-4} s⁻¹, their accumulated flux is still at a level of $\sim 10^{-12}$ erg s⁻¹ cm⁻². This is \sim two orders of magnitude lower than the observed persistent X-ray flux. Therefore, much larger contributions of smaller unresolved short bursts are required to explain the persistent X-ray flux.

For a quantitative estimate, let $N(>S)$ denote the occurrence frequency of those bursts for which the fluence is $>S$. Observationally, N is thought to be described by a single PL as $N(>S) \propto S^{-\alpha}$, as in solar flares and earthquakes. Sometimes known as the Gutenberg–Richter law, this relation is considered to represent self-organized criticality. Previous observations of SGR 1806–20 have given a range of $\alpha = 0.7$ – 1.1 ; for example, $\alpha \sim 0.9$ by the *Konus-Wind*

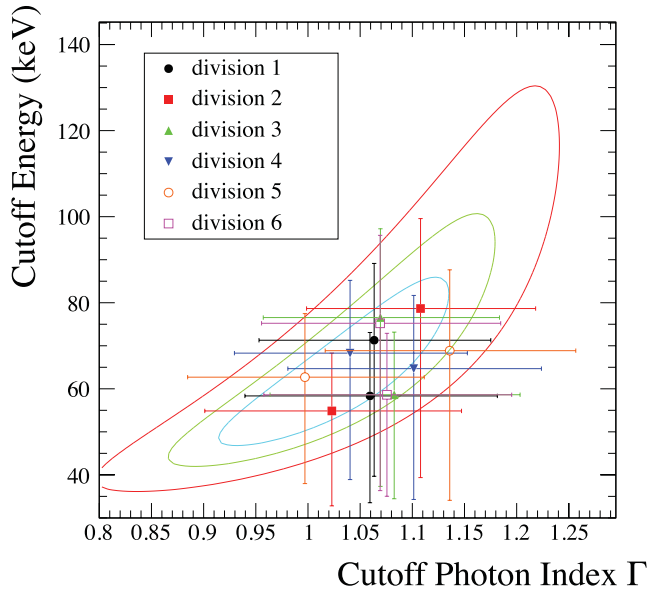


Figure 13. Confidence contours at the 68 per cent (light blue), 90 per cent (green) and 99 per cent (red) confidence levels of the CutPL fit to the stacked weak burst spectrum. Individual data points show the parameters, with $\pm 1\sigma$ errors, when the 13 short bursts are divided into two groups in six different ways.

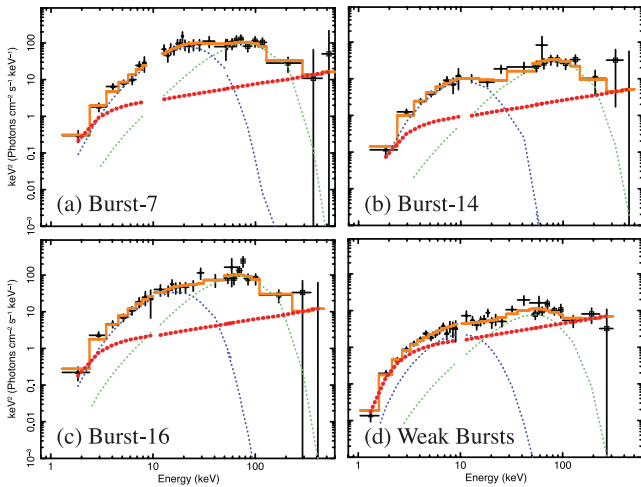


Figure 14. An νF_ν presentation of the 2BB plus PL (with $\Gamma = 1.54$ fixed) fits to the spectra of Burst-7 (a), Burst-14 (b), Burst-16 (c) and the stacked weak short bursts (d). The two BB components are represented in blue and green, while the hard PL is in red.

(Aptekar et al. 2001), $\alpha = 0.76 \pm 0.17$ by the Burst and Transient Source Experiment (BATSE), $\alpha = 0.67 \pm 0.15$ by the *International Cometary Explorer* (ICE; Göğüş et al. 2000), $\alpha = 0.91 \pm 0.09$ by *INTEGRAL* (Götz et al. 2006) and $\alpha = 1.1 \pm 0.6$ by the *High Energy Transient Explorer-2* (HETE-2; Nakagawa et al. 2007). From the present target, 1E 1547.0–5408, the slope is reported to be $\alpha = 0.75 \pm 0.06$ and $\alpha = 0.6 \pm 0.1$ using *INTEGRAL*/anticoincidence shield (ACS; Mereghetti et al. 2009) and *Swift*/X-Ray Telescope (XRT; Scholz & Kaspi 2011) observations, respectively.

The burst number density at a particular fluence S is written as $f_{\text{bst}}(S) \propto -dN(S)/dS \equiv (f_0/S_0)(S/S_0)^{-\alpha-1}$, where S_0 is a typical fluence and f_0 (burst s^{-1}) is a normalization constant. Thus, the luminosity integrated over bursts between S_1 and S_2 , at a distance d

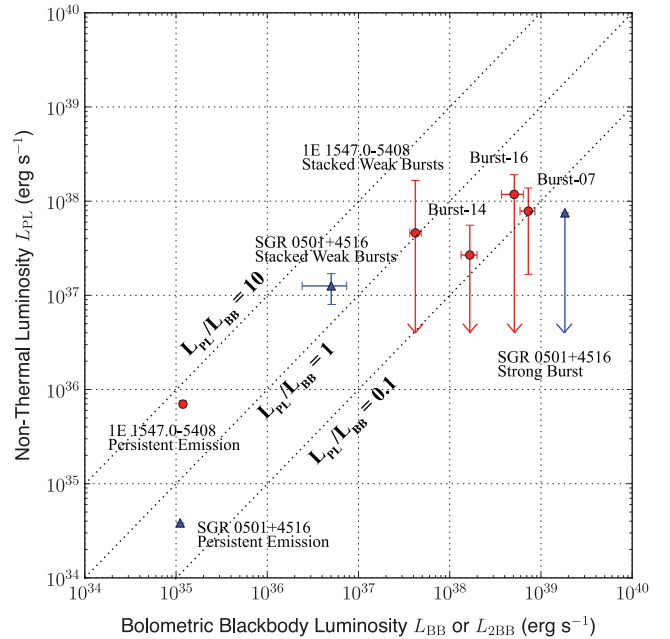


Figure 15. Comparison of the 1–300 keV PL luminosity to the bolometric BB luminosity. The results on SGR 0501+4516 were taken from fig. 8 of Nakagawa et al. (2011). In this plot, errors are shown at the 90 per cent confidence level.

(kpc), is given as

$$\begin{aligned} L_X &= \int_{S_1}^{S_2} 4\pi d^2 S f_{\text{bst}}(S) dS \\ &= 4\pi d^2 S_0 f_0 \int_{s_1}^{s_2} s^{-\alpha} ds \\ &= 4\pi d^2 S_0 f_0 \left(s_2^{1-\alpha} - s_1^{1-\alpha} \right) / (1-\alpha), \end{aligned}$$

with $s \equiv S/S_0$, $s_1 \equiv S_1/S_0$ and $s_2 \equiv S_2/S_0$. Here, let us assume $S_0 = S_{\text{min}} \sim 2 \times 10^{-9} \text{ erg cm}^{-2}$ (the present detection limit) and $s_2 = S_2/S_{\text{min}} = 1$, at $d = 4 \text{ kpc}$. The observed frequency $N(S_{\text{min}}) \sim 5.4 \times 10^{-4} \text{ burst s}^{-1}$ gives $f_0 \sim 7 \times 10^{-4} \text{ burst s}^{-1}$. In order to explain the persistent luminosity in this way, we clearly need $\alpha > 1.0$, because $S \times N \propto S^{1-\alpha}$ should increase towards smaller values of S . More quantitatively, Fig. 16 shows the calculated value of L_X as a function of α for these different values of s_1 .

Comparing the three brightest bursts and the stacked weaker bursts in Tables 2 and 3, the BB radii of the lower- or higher-temperature components are not strongly dependent on their fluence S . Thus, as a first-order approximation, let us assume $S \propto kT^4$ after the Stefan–Boltzmann law. Because the weak bursts with S_{min} and persistent emission give $kT_{\text{High}} \sim 12 \text{ keV}$ and $kT \sim 0.65 \text{ keV}$, respectively, a typical unresolved weakest burst is considered to have a fluence $s_1 = S_1/S_{\text{min}} \sim (0.65 \text{ keV}/12 \text{ keV})^4 \sim 10^{-5}$. Combined with Fig. 16, this implies that the slope α should be ~ 1.2 and ~ 1.4 to supply the luminosity of the persistent BB and PL luminosities, respectively.

The required value of $\alpha = 1.2\text{--}1.4$ is larger than has been measured. Because the observations of bursts have been performed mainly during more burst-active states than in the *Suzaku* observation, a possible interpretation is that variations of α depend on the magnetar activity. For example, the solar flare is known to change its size-distribution slope α , from ~ 0.8 at activity peaks to ~ 1.2 in more quiescent states (Bromund, McTiernan & Kane 1995). This

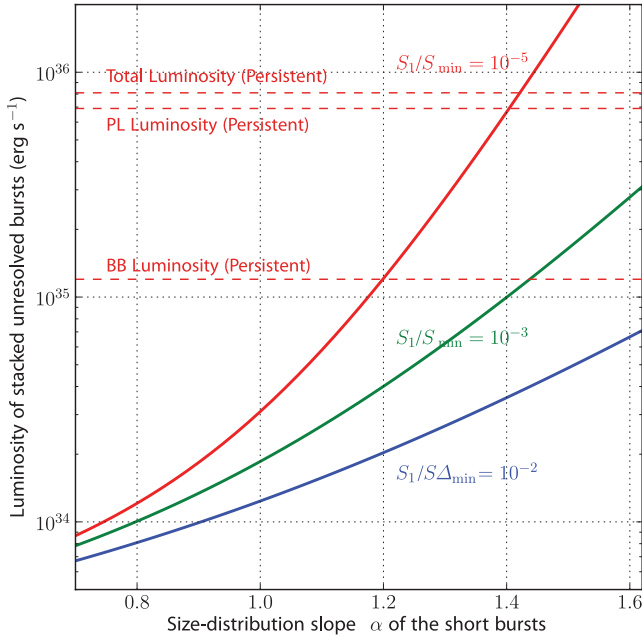


Figure 16. Expected luminosity of integrated unresolved weaker bursts, as a function of the size-distribution slope α . Blue, green and red lines are the calculations with the lower bounds of the integration at $S_1/S_{\min} = 10^{-2}$, 10^{-3} and 10^{-5} , respectively. The three horizontal lines represent the persistent X-ray luminosity of 1E 1547.0–5408 for the total (top), PL (middle) and BB (bottom) components.

is also pointed out in some magnetars (see also SGR 1806–20 and SGR 1900+14 in Nakagawa et al. 2007, related with SGR 0501+4516 behaviour in Göğüş et al. 2010b). If α reaches 1.2–1.4 in less burst-active states, the persistent emission can be explained by the superposition of microbursts. Otherwise, we infer that an alternative dissipation process, which is independent of the short-burst production, also contributes to the persistent emission. Such processes include, for example, internal crustal heating in magnetars (Aguilera, Pons & Miralles 2008).

4.3 Energy source for the emissions

Finally, let us compare the energetics of the bursts and persistent emission with the magnetic energies of magnetars. Assuming 4 kpc as before, the 2BB model and the Stefan–Boltzmann law measure the total radiated energies of 2.1×10^{38} , 1.6×10^{38} and 1.6×10^{38} erg from Burst-7, Burst-14 and Burst-16, respectively. Considering the T_{90} values further, these yield bolometric luminosities of 7.8×10^{38} , 1.9×10^{38} and 5.9×10^{38} erg s $^{-1}$, respectively. In the weaker bursts, the average energy emitted per burst becomes 1.2×10^{37} erg, and the bolometric luminosity is 4.2×10^{37} erg s $^{-1}$.

In comparison with the above estimates, the magnetic energy stored within a size of R_{mag} becomes

$$E_{\text{bst}} = \frac{B^2}{8\pi} R_{\text{mag}}^3 \text{ erg} \\ = 2 \times 10^{45} \left(\frac{B}{B_{\text{surf}}} \right)^2 \left(\frac{R_{\text{mag}}}{R_{\text{NS}}} \right)^3 \text{ erg},$$

when normalizing to the dipole magnetic field, $B_{\text{surf}} = 2.2 \times 10^{14}$ G (Camilo et al. 2007), and employing the canonical neutron star radius $R_{\text{NS}} = 10$ km. If the individual burst emission is powered by dissipation of the magnetic energy in this region (e.g. via reconnection; Lyutikov 2006), a typical size of $R_{\text{mag}} \gtrsim 10^{-2.3} R_{\text{NS}}$ is needed.

The BB radii observed in our sample (the 2BB model), $R_{\text{Low}} \sim 1$ km $= 0.1 R_{\text{NS}}$ and $R_{\text{High}} \sim 0.1$ km $= 10^{-2} R_{\text{NS}}$, are larger than the required R_{mag} . This is considered reasonable, because the released magnetic energy would, in any case, diffuse out, and would make $R_{\text{BB}} > R_{\text{mag}}$.

If we assume $s_1 \sim 10^{-5}$ and $\alpha \sim 1.4$, as in Section 4.2, the burst frequency at S_1 is estimated to be $f \sim 10^3$ Hz. Therefore, a minimum size of $R_{\text{mag}}/R_{\text{NS}} \sim 10^{-4}$ is enough to supply the observed luminosity $L_X \sim 6 \times 10^{35}$ erg s $^{-1}$, if the released magnetic energy is evaluated as $L_{\text{mag}} \sim 2 \times 10^{45} (B/B_{\text{surf}})^2 (R_{\text{mag}}/R_{\text{NS}})^3 f$ erg s $^{-1}$. Because the persistent emission exhibits $R_{\text{BB}} \sim 5$ km (Paper I), the condition of $R_{\text{BB}} > R_{\text{mag}}$ is retained.

5 CONCLUSION

We have studied short bursts from 1E 1547.0–5408 (also known as SGR J1550–5418 and PSR J1550–5418) detected during the *Suzaku* pointing observation on 2009 January 28–29 (UT) in its burst-active state. This period was 7 d after the burst forest on January 22. Combined with the previous study of its persistent X-ray emission (Paper I), we have obtained the following results.

- (i) Using a Δt distribution of the HXD-PIN data, we have identified 18 short-burst events with a risk probability below $\sim 1.7 \times 10^{-6}$. Of these, 16 that were free from data loss were used for the spectral analyses.
- (ii) The three brightest bursts have their fluences of $\sim 4\text{--}8 \times 10^{-8}$ erg cm $^{-2}$ in the 10–70 keV energy range. Their individual spectra were fitted successfully by the 2BB model (and some other models) over the 0.5 to ~ 400 keV band.
- (iii) The remaining 13 bursts define one of the weakest samples ever measured, with their fluences covering the range of 2×10^{-9} – 2×10^{-8} erg cm $^{-2}$. Their stacked spectrum is similar to the persistent emission in its slope above ~ 8 keV. This spectral similarity extends even towards lower energies, after eliminating the BB component from the persistent spectrum.
- (iv) The stacked spectrum cannot be represented by a 2BB model, while an additional hard PL made the fit acceptable, even fixing the slope at the value of the persistent emission. The luminosity of the hard PL shows signs of saturating at $\sim 10^{38}$ erg s $^{-1}$, when compared to the thermal luminosity.
- (v) We have evaluated the available energy supplied from the unresolved short bursts. The persistent emission from 1E 1547.0–5408 can be explained if the slope α of the cumulative distribution of the short bursts is steep, $\alpha = 1.2\text{--}1.4$.

ACKNOWLEDGMENTS

We thank the members of the *Suzaku* magnetar Key Project and the *Suzaku* operation teams for the successful Target of Opportunity observation (ToO). TE is supported as a Research Fellow of the Japan Society for the Promotion of Science (JSPS).

REFERENCES

- Aguilera D. N., Pons J. A., Miralles J. A., 2008, *ApJ*, 673, L167
 Aptekar R. L., Frederiks D. D., Golenetskii S. V., Il'inskii V. N., Mazets E. P., Pal'shin V. D., Butterworth P. S., Cline T. L., 2001, *ApJS*, 137, 227
 Baring M. G., Harding A. K., 2007, *Ap&SS*, 308, 109
 Bellm E., Smith D. M., Hurley K., 2009, *GRB Coordinates Network*, 8857, 1
 Beloborodov A. M., Thompson C., 2007, *Ap&SS*, 308, 631
 Bernardini F. et al., 2009, *A&A*, 498, 195
 Bernardini F. et al., 2011, *A&A*, 529, A19

- Bromund K. R., McTiernan J. M., Kane S. R., 1995, *ApJ*, 455, 733
- Camilo F., Ransom S. M., Halpern J. P., Reynolds J., 2007, *ApJ*, 666, L93
- Connaughton V., Briggs M., 2009, *GRB Coordinates Network*, 8835, 1
- den Hartog P. R., Kuiper L., Hermesen W., Kaspi V. M., Dib R., Knödseder J., Gavriil F. P., 2008, *A&A*, 489, 245
- den Hartog P. R., Kuiper L., Hermesen W., 2009, *The Astronomer's Telegram*, 1922, 1
- Duncan R. C., Thompson C., 1992, *ApJ*, 392, L9
- Enoto T. et al., 2009, *ApJ*, 693, L122
- Enoto T. et al., 2010a, *ApJ*, 715, 665
- Enoto T. et al., 2010b, *PASJ*, 62, 475 (Paper I)
- Enoto T., Nakazawa K., Makishima K., Rea N., Hurley K., Shibata S., 2010c, *ApJ*, 722, L162
- Enoto T., Makishima K., Nakazawa K., Kokubun M., Kawaharada M., Kotoku J., Shibazaki N., 2011, *PASJ*, 63, 387
- Esposito P. et al., 2011, *MNRAS*, 416, 205
- Fernández R., Thompson C., 2007, *ApJ*, 660, 615
- Feroci M., Hurley K., Duncan R. C., Thompson C., 2001, *ApJ*, 549, 1021
- Fukazawa Y. et al., 2009, *PASJ*, 61, 17
- Gavriil F. P., Kaspi V. M., Woods P. M., 2004, *ApJ*, 607, 959
- Gelfand J. D., Gaensler B. M., 2007, *ApJ*, 667, 1111
- Golenetskii S., Aptekar R., Mazets E., Pal'Shin V., Frederiks D., Oleynik P., Ulanov M., Cline T., 2009, *GRB Coordinates Network*, 8863, 1
- Gotthelf E. V., Halpern J. P., 2005, *ApJ*, 632, 1075
- Gotthelf E. V., Halpern J. P., Buxton M., Bailyn C., 2004, *ApJ*, 605, 368
- Götz D. et al., 2006, *A&A*, 445, 313
- Göğüş E., Woods P. M., Kouveliotou C., van Paradijs J., Briggs M. S., Duncan R. C., Thompson C., 2000, *ApJ*, 532, L121
- Göğüş E., Kouveliotou C., Woods P. M., Thompson C., Duncan R. C., Briggs M. S., 2001, *ApJ*, 558, 228
- Göğüş E. et al., 2010a, *ApJ*, 718, 331
- Göğüş E., Woods P. M., Kouveliotou C., Kaneko Y., Gaensler B. M., Chatterjee S., 2010b, *ApJ*, 722, 899
- Graziani C., 2003, in Ricker G. R., Vanderspek R. K., eds, *Proc. AIP Conf. Vol. 662, Gamma-Ray Burst and Afterglow Astronomy 2001: A Workshop Celebrating the First Year of the HETE Mission*. Am. Inst. Phys., New York, p. 79
- Gronwall C., Holland S. T., Markwardt C. B., Palmer D. M., Stamatikos M., Vetere L., 2009, *GRB Coordinates Network*, 8833, 1
- Halpern J. P., Gotthelf E. V., Reynolds J., Ransom S. M., Camilo F., 2008, *ApJ*, 676, 1178
- Heyl J. S., Hernquist L., 2005, *MNRAS*, 362, 777
- Hurley K. et al., 2005, *Nat*, 434, 1098
- Ibrahim A. I. et al., 2004, *ApJ*, 609, L21
- Israel G. L. et al., 2004, *ApJ*, 603, L97
- Israel G. L., Campana S., Dall'Osso S., Muno M. P., Cummings J., Perna R., Stella L., 2007, *ApJ*, 664, 448
- Israel G. L. et al., 2008, *ApJ*, 685, 1114
- Israel G. L. et al., 2010, *MNRAS*, 408, 1387
- Kaneko Y. et al., 2010, preprint (arXiv:1001.2644)
- Kargaltsev O. et al., 2012, *ApJ*, 748, 26
- Kouveliotou C. et al., 2001, *ApJ*, 558, L47
- Kouveliotou C., von Kienlin A., Fishman G., Connaughton V., van der Horst A., Bhat N., 2009, *GRB Coordinates Network*, 8915, 1
- Koyama K. et al., 2007, *PASJ*, 59, 23
- Kuiper L., Hermesen W., den Hartog P. R., Collmar W., 2006, *ApJ*, 645, 556
- Kuiper L., den Hartog P. R., Hermesen W., 2009, *The Astronomer's Telegram*, 1921, 1
- Lamb R. C., Markert T. H., 1981, *ApJ*, 244, 94
- Lyutikov M., 2003, *MNRAS*, 346, 540
- Lyutikov M., 2006, *MNRAS*, 367, 1594
- Matsuta K. et al., 2009, in *Proc. Suzaku Conf.*, *The Energetic Cosmos: from Suzaku to ASTRO-H*. Japan Aerospace Exploration Agency, JAXA-SP-09-008E, p. 412
- Matsuta K. et al., 2010, Recipe for reducing XIS data taken with the P-sum/timing mode, http://www.astro.isas.ac.jp/suzaku/analysis/xis/psum_recipe/Psum-recipe-20100724.pdf
- Mazets E. P., Golentskii S. V., Ilinskii V. N., Aptekar R. L., Guryan I. A., 1979, *Nat*, 282, 587
- Mereghetti S., 2008, *A&A Rev.*, 15, 225
- Mereghetti S. et al., 2009, *ApJ*, 696, L74
- Muno M. P., Gaensler B. M., Clark J. S., de Grijs R., Pooley D., Stevens I. R., Portegies Zwart S. F., 2007, *MNRAS*, 378, L44
- Nakagawa, 2007, PhD Thesis, Aoyama Gakuin University
- Nakagawa Y. E. et al., 2007, *PASJ*, 59, 653
- Nakagawa Y. E., Yoshida A., Yamaoka K., Shibazaki N., 2009, *PASJ*, 61, 109
- Nakagawa Y. E., Makishima K., Enoto T., 2011, *PASJ*, 63, S813
- Ng C.-Y. et al., 2011, *ApJ*, 729, 131
- Olive J.-F. et al., 2004, *ApJ*, 616, 1148
- Paczynski B., 1992, *A&A*, 42, 145
- Rea N., Turolla R., Zane S., Tramacere A., Stella L., Israel G. L., Campana R., 2007, *ApJ*, 661, L65
- Rea N. et al., 2009, *MNRAS*, 396, 2419
- Rea N. et al., 2010, *Sci*, 330, 944
- Rea N. et al., 2012, *ApJ*, 754, 27
- Savchenko V., Beckmann V., Neronov A., Mereghetti S., von Kienlin A., Beck M., Borkowski J., Götz D., 2009, *GRB Coordinates Network*, 8837, 1
- Scholz P., Kaspi V. M., 2011, *ApJ*, 739, 94
- Sugizaki M., Mitsuda K., Kaneda H., Matsuzaki K., Yamauchi S., Koyama K., 2001, *ApJS*, 134, 77
- Takahashi T. et al., 2007, *PASJ*, 59, 35
- Terada Y. et al., 2008, *PASJ*, 60, 25
- Terada Y. et al., 2009, *GRB Coordinates Network*, 8845, 1
- Thompson C., Beloborodov A. M., 2005, *ApJ*, 634, 565
- Thompson C., Duncan R. C., 1995, *MNRAS*, 275, 255
- Thompson C., Duncan R. C., 1996, *ApJ*, 473, 322
- Thompson C., Lyutikov M., Kulkarni S. R., 2002, *ApJ*, 574, 332
- Tiengo A. et al., 2010, *ApJ*, 710, 227
- van der Horst A. J. et al., 2010, *ApJ*, 711, L1
- van der Horst A. J. et al., 2012, *ApJ*, 749, 122
- von Kienlin A., Connaughton V., 2009, *GRB Coordinates Network*, 8838, 1
- Woods P. M., Thompson C., 2006, in Lewin W., van der Klis M., eds, *Compact Stellar X-ray Sources*. Cambridge Univ. Press, Cambridge, p. 547

APPENDIX A: CORRECTION FOR THE P-SUM MODE XIS0

Here, we describe further calibrations of the time assignments and responses of the P-sum (timing) mode XIS0, dedicated to the present analyses.

A1 Timing correction

It is known that there is still a slight time lag (~ 30 ms) assigned to the P-sum mode of the XIS, even after including corrections related with readout time delays, depending on the source position on the XIS CCD chip (see Matsuta et al. 2009). To study the burst light curves in detail, we have further assigned an additional timing correction to the P-sum mode, comparing the HXD-PIN data, which have already been accurately calibrated using the Crab pulsar (Terada et al. 2008). In order to evaluate the residual time lag, we have compared the burst light curves of the XIS0 to those of the HXD-PIN, both in 10–14 keV. We have accumulated five short bursts, in which the 10–14 keV photons were clearly detected in the HXD-PIN data. The left panels of Fig. A1 are the 10–14 keV cumulative light curves of XIS0 and HXD-PIN, respectively, while the right panels of Fig. A1 are the 40–70 keV cumulative light curves of HXD-PIN and HXD-GSO as a reference. As compared here, the 40–70 keV

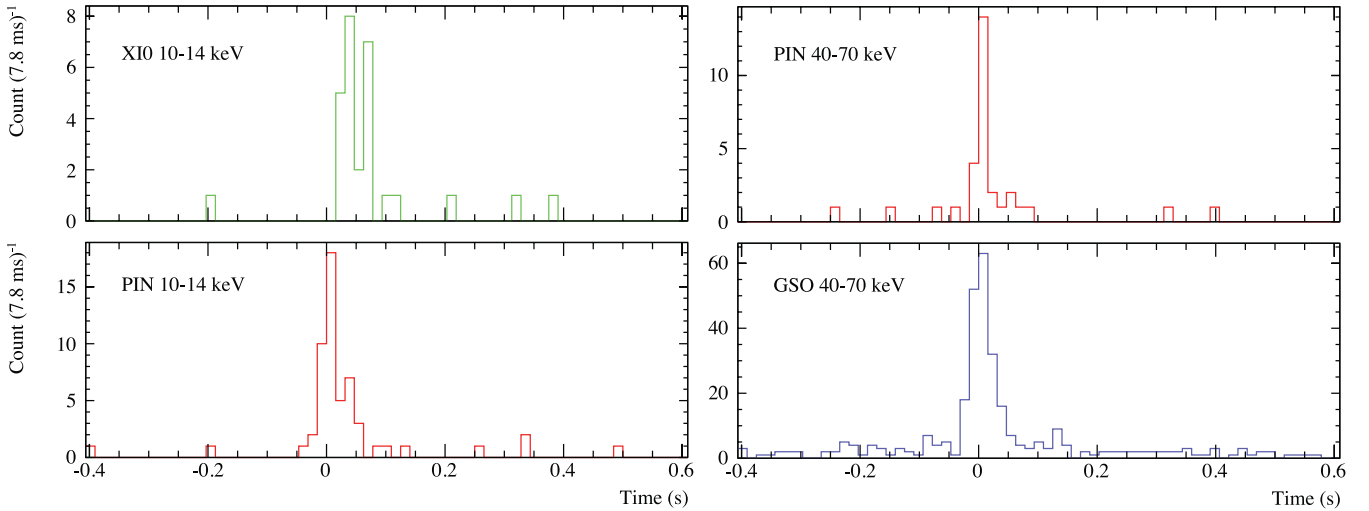


Figure A1. Left: accumulated light curves of five short bursts (Burst-4, Burst-7, Burst-9, Burst-14 and Burst-16) from XIS0 (top) and HXD-PIN (bottom), both in the 10–14 keV energy range. Right: same as the left panels, but from HXD-PIN (top) and HXD-GSO (bottom), both in the 40–70 keV energy range. Burst-2, Burst-6, Burst-7, Burst-9, Burst-10, Burst-11, Burst-14, Burst-16 and Burst-18 are used for the accumulation.

peaks correspond with each other, while the peak of the 10–14 keV XIS0 data comes slightly later than that of the HXD-PIN data.

In order to quantitatively evaluate this XIS0 time lag, we calculated the cross-correlations. The cross-correlation coefficient $R_{xy}(i)$ for the i th bin is calculated by

$$R_{xy}(i) = \frac{1}{N-i} \sum_{j=0}^{N-1-i} x(j)y(i+j) \quad (i = 0, 1, \dots, N-1). \quad (\text{A1})$$

Figs A2(a) and (b) show the cross-correlation coefficients of the 10–14 and 40–70 keV data, respectively. As clearly shown in these figures, no time lag was confirmed between the HXD 40–70 keV data (Fig. A2b), while the cross-correlation peak of the 10–14 keV range appears at 31.25 ms in Fig. A2(a). Thus, we have assigned the time correction of 31.25 ms to the XIS0 data set ($\text{TIME} - 0.0325$ s). This correction is consistent with the previous analyses of the persistent X-ray emission in section 3.1 of Paper I. The individual light curves of XIS0 in Fig. 5 have already been corrected for this time lag of 31.25 ms.

A2 Response correction

For the XIS0 spectral analyses, we have produced RMFs and ARFs based on the procedure stated by Matsuta et al. (2010). Because the P-sum spectral data have not been widely utilized so far, careful calibration is necessary. We have also included correction factors to the RMFs and ARFs, as follows. The persistent X-ray emission from 1E 1547.0–5408 was already measured using the XIS1, XIS3, HXD-PIN and HXD-GSO data in Paper I. We have also produced the same persistent X-ray spectra from the XIS0, after eliminating bright short bursts, and we have compared these with Paper I. We have fixed the spectral parameters at the values reported in Paper I, and only three parameters of the XIS0 response (a normalization factor, a slope and an offset of the gain) were left free to be fitted. We have determined the normalization factor, the slope and the gain to be 1.079, 0.90 and -0.05 , respectively. In this paper, we use these correction factors.

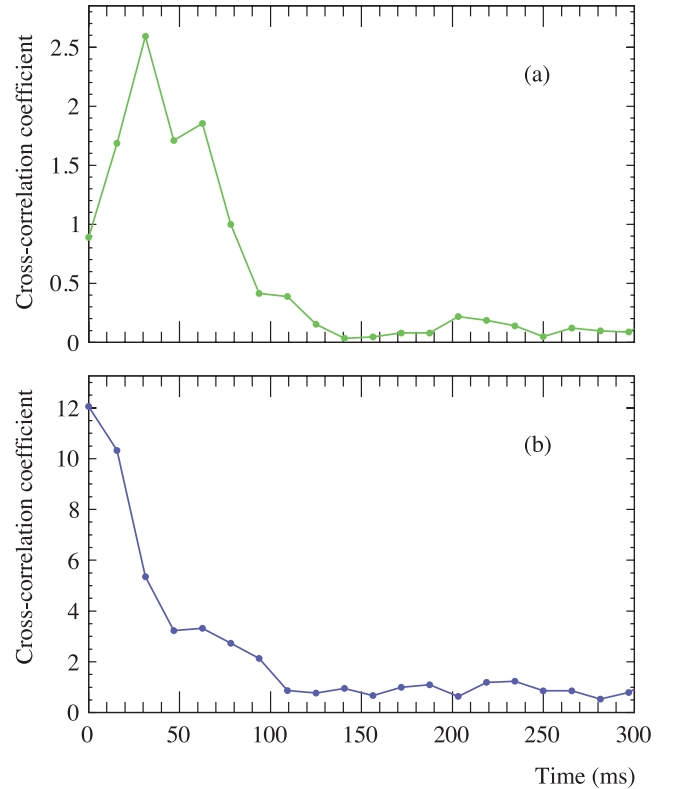


Figure A2. Cross-correlation coefficients calculated using equation (A1): (a) obtained from the P-sum mode XIS0 data to the HXD-PIN data, both in the 10–14 keV energy range, corresponding to the data in the left panels of Fig. A1; (b) obtained from the HXD-GSO data to the HXD-PIN data, both in the 40–70 keV energy range, corresponding to those in the right panels of Fig. A1.

APPENDIX B: STATISTICAL SIGNIFICANCES OF DETECTED BURSTS

We have already evaluated the detection significances in Section 2.2 using only the HXD-PIN data. Here, we evaluate the statistical significance of these detections further, by combining the XIS,

HXD-PIN and HXD-GSO data together. In particular, the XIS instruments are placed at different locations in the *Suzaku* satellite, and temporal coincidences of the X-ray events between the HXD and the XIS0 make the detection much more plausible. The possibility of detecting n events, from the Poisson distribution of its average λ count s^{-1} , during a time duration of T , can be written as $P(\lambda, n) = (\lambda T)^n \exp(-\lambda T)/n!$. Thus, multiplied by the independent instruments, the total probability of these bursts becomes $P_{\text{total}} = P_{\text{XIS}} P_{\text{PIN}} P_{\text{GSO}}$. Here, we employ $T = 1$ s and the corresponding burst rates listed in Table 1, together with the average rate of $\lambda_{\text{XIS0}} = 3.98$ counts s^{-1} , $\lambda_{\text{PIN}} = 0.76$ counts s^{-1} and $\lambda_{\text{GSO}} = 13.38$ counts s^{-1} (see Section 2.1). Considering the total bin number of $n_{\text{bin}} = 4.5 \times 10^4$, the chance occurrence $n_{\text{bin}} P_{\text{total}}$ of these bursts is estimated to be below 10^{-5} . Therefore, we have confirmed these events are indeed short bursts.

APPENDIX C: CHECK OF THE DATA LOSS

The burst data (except for Burst-6 and Burst-10) have been examined for possible losses or pile ups, using the same procedure as applied to the much brighter burst from SGR 0501+4516, recorded

with *Suzaku* in 2008 (Enoto et al. 2009). There are three possible forms of data loss: (i) dead time in the event handling at the analogue electronics (HXD-AE); (ii) the limited event transfer rate from HXD-AE to the digital electronics (HXD-DE); (iii) the limited event transfer rate from HXD-DE to the spacecraft data processor. Because the peak count rates of these bursts are less than ~ 60 counts $(15.6 \text{ ms})^{-1}$, the effect of (i) is estimated to be, at most, $\lesssim 8$ per cent, and on average ~ 1 per cent, because the data acquisition time ($20 \mu\text{s}$) is much shorter than the burst event interval. Pile up is much less effective because of a short time window for the pulse height latch. These event data were not lost in the (ii) and (iii) processes, because the event rates were much smaller than the maximum limits: 4 kHz for (ii) and 400 counts $(4 \text{ s})^{-1}$ for (iii). Thus, our samples are free from data loss as a result of dead time or event pile ups. Because the dead-time effect is typically ~ 1 per cent for most cases, we do not correct for the dead time.

This paper has been typeset from a \LaTeX file prepared by the author.